

UNIVERSITY of CALIFORNIA
SANTA CRUZ

**CONSTRAINING TYPE Ia SUPERNOVA PROGENITOR
SCENARIOS WITH EXTREMELY LATE-TIME PHOTOMETRY OF
SUPERNOVA SN 2013aa**

A thesis submitted in partial satisfaction of the
requirements for the degree of

BACHELOR OF SCIENCE

in

PHYSICS

by

Wynn V. Jacobson-Galán

15 June 2018

The thesis of Wynn V. Jacobson-Galán is approved by:

Professor Ryan Foley
Advisor

Professor Alexander Sher
Senior Theses Coordinator

Professor Robert Johnson
Chair, Department of Physics

Copyright © by

Wynn V. Jacobson-Galán

2018

Abstract

Constraining Type Ia Supernova Progenitor Scenarios with Extremely Late-time Photometry of Supernova SN 2013aa

by

Wynn V. Jacobson-Galán

We present *Hubble Space Telescope* observations and photometric measurements of the Type Ia supernova (SN Ia) SN 2013aa 1500 days after explosion. At this epoch, the luminosity is primarily dictated by the amounts of radioactive ^{57}Co and ^{55}Fe , while at earlier epochs, the luminosity depends on the amount of radioactive ^{56}Co . The ratio of odd-numbered to even-numbered isotopes depends significantly on the density of the progenitor white dwarf during the SN explosion, which, in turn, depends on the details of the progenitor system at the time of ignition. From a comprehensive analysis of the entire light curve of SN 2013aa, we measure a $M(^{57}\text{Co})/M(^{56}\text{Co})$ ratio of $0.02_{-0.02}^{+0.01}$, which indicates a relatively low central density for the progenitor white dwarf at the time of explosion, consistent with double-degenerate progenitor channels. We estimate $M(^{56}\text{Ni}) = 0.732 \pm 0.151 M_{\odot}$, and place an upper limit on the abundance of ^{55}Fe . Being the fifth SNe Ia with a late-time detection of radioactive decay channels and the second latest photometric detection, SN 2013aa will add to the larger sample of SNe Ia while also aiding in our understanding of these unique stellar explosions.

Contents

Acknowledgements	v
1 Introduction	1
1.1 Overview of Type Ia Supernova	1
1.2 Explosion Models	6
1.3 Light Curves of SNe Ia	9
1.4 Late-time Studies of SNe Ia	10
2 Observations	12
2.1 Early-time Data (up to 400 days)	12
2.2 Hubble Space Telescope (HST) Data	14
3 Analysis	20
3.1 Constructing a Pseudo-Bolometric Light Curve	20
3.2 The Bolometric Light Curve Model	21
3.3 Results from Light-Curve Model Fitting	24
4 Discussion	28
4.1 Comparison to Explosion Models	28
4.2 Comparison to Other Supernova Observed at Late-Time Epochs	29
4.3 Non-Optical Contribution to the Bolometric Luminosity	32
4.4 Companion Contamination?	33
4.5 Light Echoes?	33
5 Conclusions	35
6 Tables	37

Acknowledgements

First and foremost, I would like to acknowledge all that Professor Ryan Foley has done for my research career thus far. Ryan has provided me with opportunities to pursue aspects of astrophysics that I could not have imagined possible prior to transferring to UCSC. My passion for observational astrophysics has been greatly influenced by Ryan's faith in my research and for that I am forever grateful. Secondly, I cannot give enough thanks to Postdoctoral Scholars Charlie Kilpatrick and Georgios Dimitriadis; their willingness to answer my countless questions as well as provide insight on supernovae science has been a crucial component of this research. I would also like to thank all of my family and friends who have shown me unconditional support throughout my tumultuous yet rewarding undergraduate path. And last, but certainly not least, I express my overwhelming gratitude for my incredible girlfriend who has shown me nothing but love in spite of all the madness. Science truly is a community effort and it is beautiful to witness all that we can accomplish together.

“There is a new quality in the Universe, which exists only because there are human beings. Physicists must from now on, when pondering the secrets of the Cosmos, factor in not only energy and matter and time, but something very new and beautiful, which is *human awareness*.”

- Kilgore Trout

To a girl and her cat.

1 Introduction

Type Ia Supernova (SNe Ia) are the product of a thermonuclear explosion involving a carbon-oxygen white dwarf in a binary system [1]. During explosion, these impressive events synthesize heavy elements such as Nickel, Cobalt and Iron, the result of which has significant effect on the chemical evolution of galaxies. Furthermore, in the past two decades, the luminosity of SNe Ia has been standardized to the point that they can be used as distance indicators in our observable universe [2]. This corrective process has led to the measurement of the accelerating universe as well as the study of vacuum energy i.e., “dark energy” [3; 4]. However, despite the advancements in astrophysics attributed to SNe Ia, the progenitor system prior to explosion still remains a mystery. In recent years, two proposed models have attempted to describe the binary star system responsible for SNe Ia: the single-degenerate (SD) model, in which a near-Chandrasekhar mass white dwarf accretes material from a more massive binary companion until it explodes at the mass limit, and the double-degenerate (DD) model where two, sub-Chandra mass white dwarfs merge violently. Both models showing promise as well as problems, it is crucial to the further application of SNe Ia that we answer the question of the SNe Ia progenitor system.

1.1 Overview of Type Ia Supernova

Supernovae are stellar explosions whose peak luminosity can outshine entire galaxies several times over. These explosions have a variety of subclassifications based on the specifics of the explosion e.g., the progenitor star(s), elemental signatures or explosive mechanism. The various families of

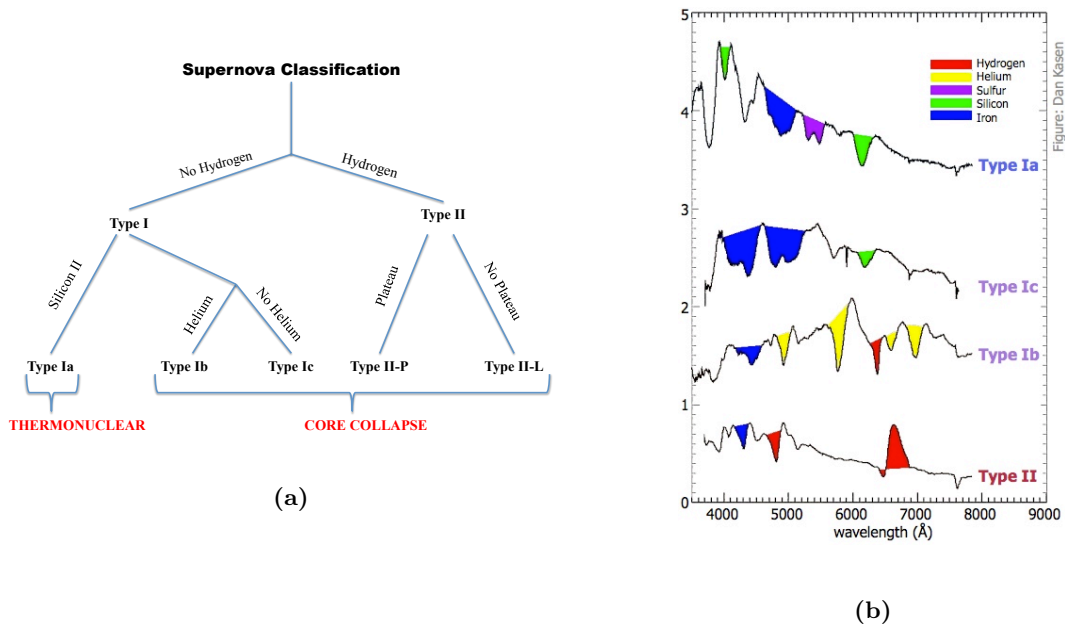


Figure 1.1: (a) Supernova family tree. (b) Different classifications of supernovae based on variations in observed spectra. Y-axis in arbitrary flux units. Source: Dan Kasen (<http://supernova.lbl.gov/dnkasen/tutorial/>)

supernova are shown in Figure 1.1. This work will focus on Type Ia Supernova (SNe Ia), which are the result of a thermonuclear explosion of a carbon-oxygen white dwarf (WD) in a binary star system [1; 5; 6]. Within observational surveys, SNe Ia comprise $\sim 24\%$ of observed supernova explosions and are distinguished by a lack of Hydrogen emission lines in their spectra [7]. Additional spectral features include prominent, blueshifted Silicon absorption lines known as the 6150\AA feature. Based on observed relations between host galaxies and the luminosities of these stellar explosions, SNe Ia with higher peak magnitudes and a slower decline in their luminosity are typically found in later type galaxies e.g., spiral or irregular galaxies [8; 9]. However, SNe Ia with fainter peak luminosities prefer earlier type elliptical galaxies e.g., E/S0 [10; 11]. The detection of SNe Ia in elliptical galaxies containing stellar populations older than 1 Gyr implies that SNe Ia are the result of low mass stars rather than the death of more massive stars.

Based on observational samples, $\sim 70\%$ of discovered SNe Ia are characterized as “normal” due to their similar light curve shape and luminosity decline rate [12]. This relative consistency led to the creation of the Phillips Relation, which is a fitted trend of peak absolute B-band magnitude versus luminosity decline rate as observed in SNe Ia [13]. This fitted relation is shown in Figure 1.2. While the Phillips Relation is an important categorization of normal SNe Ia, other, non-standard SNe Ia are also considered when studying this subclass of stellar explosion. Also displayed in Figure 1.2, varieties of SNe Ia have been discovered and characterized based on their luminosity and light curve evolutions. For example, 91T-like SNe Ia are supernovae that share similarities to discovered SNe Ia SN 1991T, which was significantly over-luminous and had a slow-to-normal decline rate in its luminosity. 91T-like supernovae comprise $\sim 9\%$ of discovered SNe Ia. Other peculiar SNe Ia that do not fit the Phillips Relation are SNe Iax, which all share similar spectroscopic features to SN 2002cx. These supernovae make up $\sim 5\%$ of the known SNe Ia sample and possess relatively low luminosities compared to normal SNe Ia. This process of classifying all strains of SNe Ia is a paramount effort due to the applications of SNe Ia in studying large scale structure in our universe. All other known categories of SNe Ia are presented in the left panel of Figure 1.2.

In the realm of cosmology, SNe Ia are known as “standard candles” as a result of their relatively consistent luminosities during explosion. However, as is shown in Figure 1.2, SNe Ia are not completely standard, but rather standardizable. It has been estimated that there is at least a 40% initial difference in SNe Ia luminosity evolution prior to correction [14]. Nonetheless, by applying corrections for stretch (light curve broadness) and intrinsic color differences, the variation in brightness drops to $\sim 15\%$ [13]. The stretch correction can be applied to both normal and peculiar SNe Ia because it relies on the fact that over luminous supernovae (e.g., 91T-like) have broader light curves and decline slower, while less luminous SNe Ia (e.g., 91bg-like) have narrower, faster declining light curves; this being a key aspect of SNe Ia standardization. This is shown in the right panel of Figure 1.2.

This process of standardizing SNe Ia light curves has had an incredible influence on our

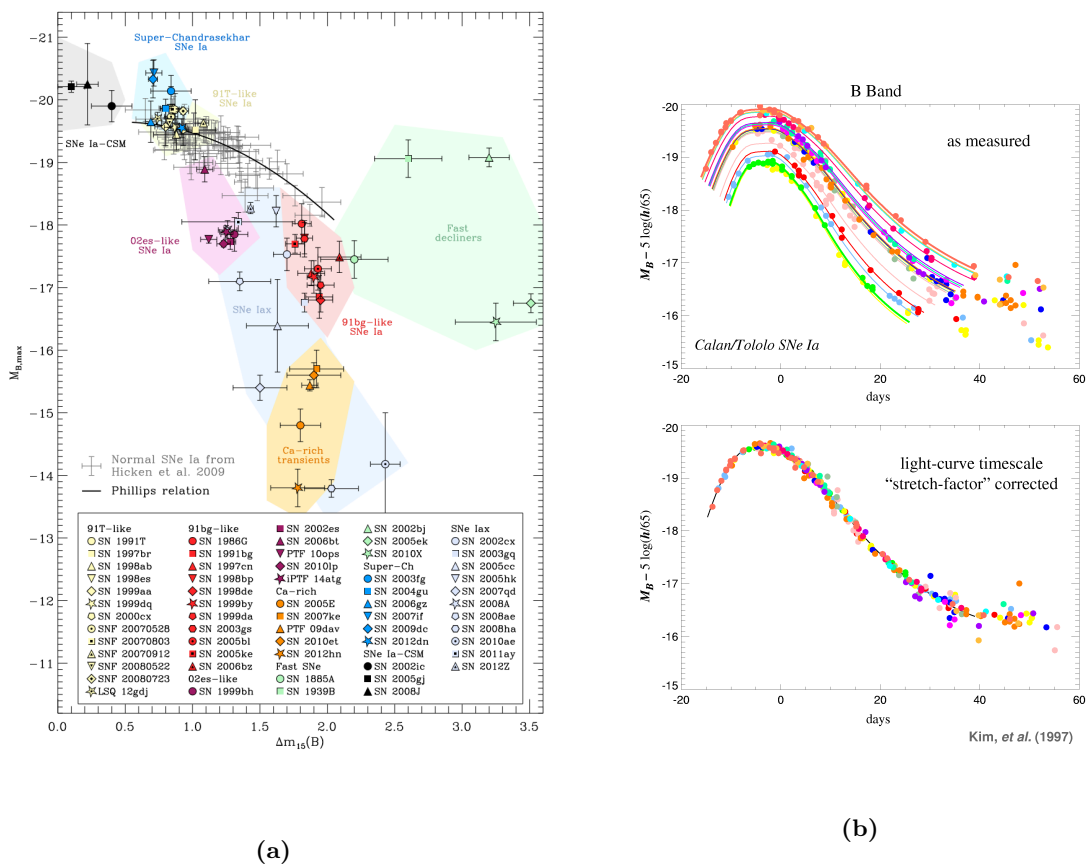


Figure 1.2: (a) Absolute magnitude vs. decline rate in B-band 15 days after peak ($\Delta m_{15}(B)$) of various Type Ia Supernova with fitted Phillips Relation to normal SNe Ia. Colored regions represent different groupings of SNe Ia. Plot taken from Figure 1 of Taubenberger (2017) [15] (b) Stretch corrected SNe Ia light curves. Colored lines represent fitted functions to the photometry data points. Figure taken from the Supernova Cosmology Project. [14]

understanding of modern cosmology. Since the 1990's, the reduction in light curve variation between SNe Ia has allowed for these objects to be applied as distance metrics in the observable universe. Riess et al. (1996) standardized SNe Ia via the Multi-Color Light Curve Shape method (MLCS). This approach defines the shape of the SNe Ia light curve as a function of peak magnitude, as well as allows for multi-band light curve fits and dust extinction measurements [2]. An alternative approach for standardizing SNe Ia was the stretch method as employed by Perlmutter et al. (1997).

This method analyzes the entire length of the light curve while allowing for the time axis stretch factor to be fit as a free variable [16; 17]. These standardization techniques have yielded amazing success in cosmological measurements, the most monumental being the discovery of the accelerating universe using SNe Ia by Riess et al (1998) and Perlmutter et al. (1999) [3; 4]. This has led to the ongoing study of the mysterious effects of “dark energy” on the expansion of the universe. While the applications of SNe Ia as cosmological probes are far reaching, the exact nature of the explosion and the progenitor system, and in particular the binary companion, are still an open question [see e.g., 18]. Understanding the process that generates SNe Ia is extremely important in reducing uncertainties in cosmology calculations, as well as adding to our larger understanding of stellar evolution.

There are several ways to potentially produce a SN Ia, and in each SNe Ia progenitor scenario prior to explosion, there exists at least one white dwarf star [19]. This stellar object is an extremely dense remnant of a stellar core produced at the end of the main sequence stellar lifecycle. When a main sequence star ($0.5 - 8 M_{\odot}$) has completed its fusion of helium into carbon and oxygen, it sheds its outer layers of stellar material until all that is left is a carbon-oxygen core [20]. While higher mass stars ($8 - 10 M_{\odot}$) may generate neutron stars, this specific process yields a densely packed, carbon-oxygen white dwarf star that can be the progenitor star responsible for a SN Ia explosion. White dwarfs can come in a variety of sizes but cannot exceed the Chandrasekhar mass limit ($\sim 1.44 M_{\odot}$). This is the maximum mass a stable WD can have due to the fact that its gravitational collapse is balanced by electron degeneracy pressure below a mass of $\sim 1.44 M_{\odot}$ [21]. However, for the case of SNe Ia, the progenitor WD is in a binary star system with a companion star. Based on our current understanding of SN Ia explosions, the mass of the primary WD varies based on the binary companion.

1.2 Explosion Models

Within high-energy astrophysics, there is a relatively even split between theoretical models of SNe Ia explosions. In some similar models, the (primary) WD is very close to the Chandrasekhar mass and possesses a high central density ($\sim 3 \times 10^9 \text{ g cm}^{-3}$), having undergone a simmering stage [22] in which the convective region expands to encompass $\sim 1 M_{\odot}$ of the WD [23]. However, in alternate models, the primary and/or secondary WD is below the Chandrasekhar mass and contains a low central density ($\sim 2 \times 10^6 \text{ g cm}^{-3}$) [24]. The details of the explosive nuclear burning depends critically on the central density. In particular, explosions with higher central densities will produce more Fe-group elements with an odd number of nucleons [25; 26]. Since some of the isotopes produced are radioactive, measuring the mass of these isotopes can be applied to a calculation of central density, which can in turn distinguish between explosion models.

In addition to different explosions, there are fundamentally different progenitor channels for the generation of SNe Ia. Accompanying the WD in the binary system, the single-degenerate (SD) channel has a non-degenerate main sequence (or larger) companion star, while the double-degenerate (DD) channel has an additional, sub-Chandrasekhar WD companion. The DD channel will naturally possess a sub-Chandrasekhar mass primary and a relatively low central density. While some SD systems might result in a sub-Chandrasekhar mass explosion, the classical model involves a Chandrasekhar-mass WD and a high central density. The single-degenerate (SD) model argues that the explosion is triggered by a high central density, delayed detonation of a near-Chandrasekhar-mass WD as it accretes material and energy from main-sequence or larger star [28; 29]. As a result of the variability of this explosion scenario, there are a variety of SD models that attempt to probe physical causes for SNe Ia. For example, the pure deflagration scenario contends that the initial, subsonic nuclear burning consumes all Carbon and Oxygen before subsonic detonation occurs at the Chandrasekhar mass. This model can be ruled out if any amount of Carbon or Oxygen remains post-explosion just as a pure detonation SD model can be ruled out if there remains any heavy elements such as Iron or Nickel. The latter is not a popular scenario considering how crucial the role

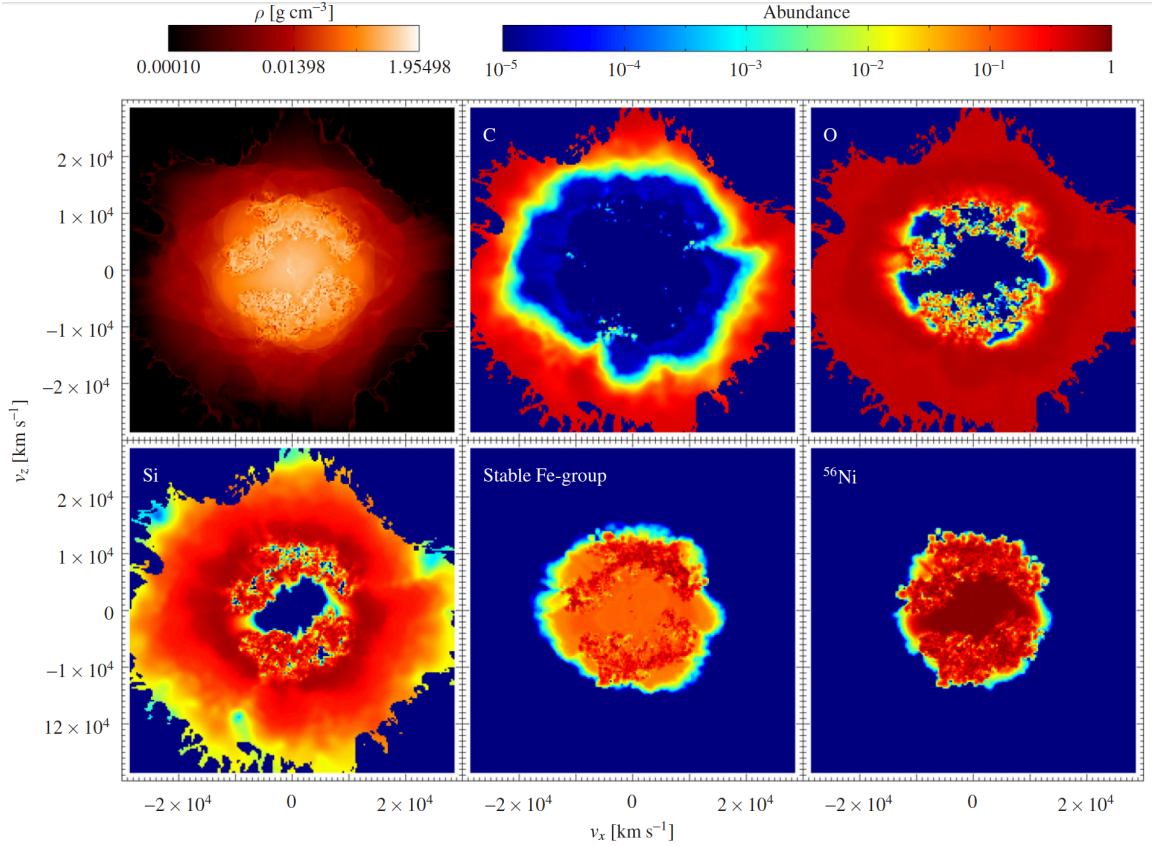


Figure 1.3: Hydrodynamical simulation of a high central density, single-degenerate (SD) explosion model involving a Chandrasekhar mass white dwarf and a main sequence or larger companion. Rainbow abundance color bar indicates the isotope mass while the red color bar presents the central density evolution. Blue panels represent different elements synthesized during explosion. Axis labels present the ejecta velocity during explosion. Plot taken from Figure 1 of Röpke et al. (2012) [27]

of Nickel and Iron isotopes are in the SNe Ia luminosity. Other SD variations include detonations below the Chandra-mass limit. Additionally, SD models do not have to only involve a C-O WD, for many sub-Chandra WDs in SD models are C-O-Ne WDs whose Helium layer results in a secondary detonations after deflagration occurs. These specific hydrodynamical SD models are presented in Section 4.2.

Alternatively, the double-degenerate (DD) model consists of a low central density, violent

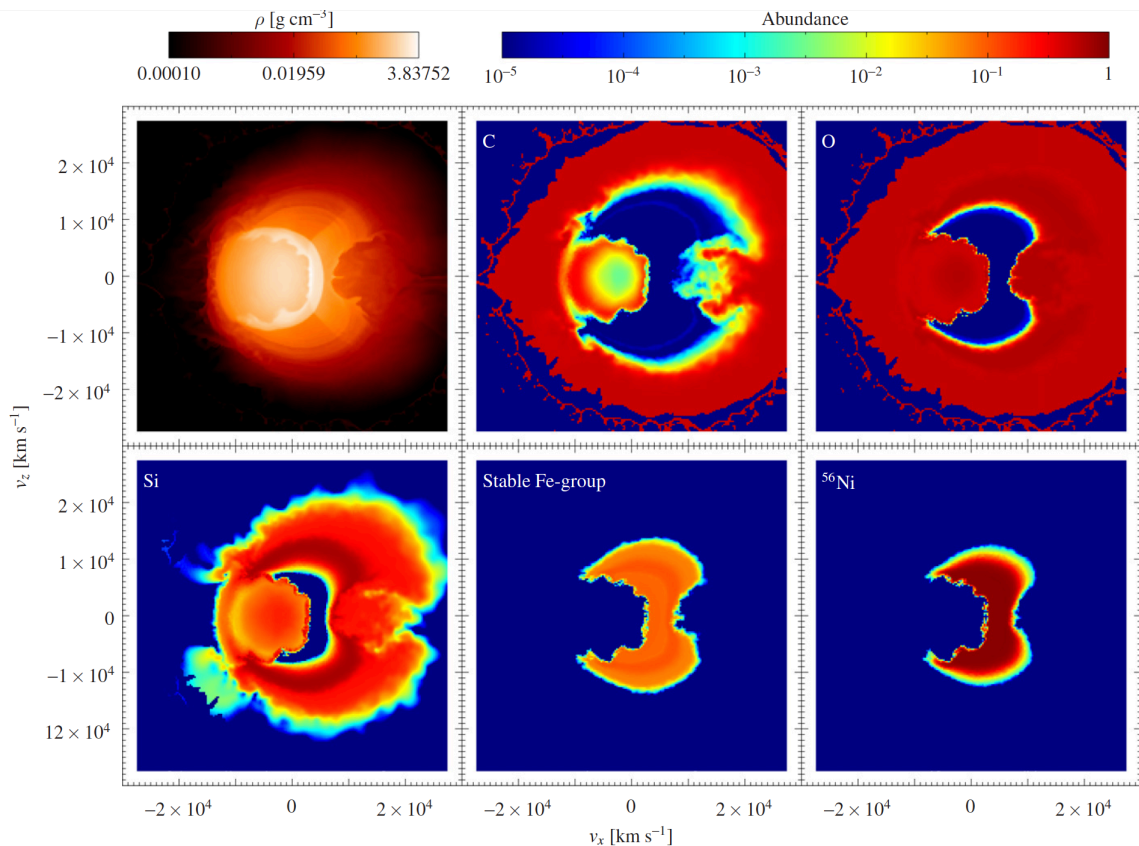


Figure 1.4: Low central density, double-degenerate model demonstrating the violent merger of two sub-Chandra white dwarf stars. Rainbow abundance color bar indicates the isotope mass while the red color bar presents the central density evolution. Blue panels represent different elements synthesized during explosion. Axis labels present the ejecta velocity during explosion. Plot taken from Figure 2 of Röpke et al. (2012) [27]

merger of two, sub-Chandrasekhar-mass WD stars [30; 31]. In this progenitor channel, two WDs orbit a common center of mass and eventually begin to lose angular momentum due to gravitational interaction. This then causes the WDs to collide and ignites the carbon fusion process responsible for SNe Ia luminosity. Just as with the SD models, DD models present a range of possible scenarios involving a double white dwarf binary system. All DD models begin with below Chandra-mass WDs, but the combination of masses varies from model to model. Furthermore, the metallicity

of each WDs i.e., the amount of elements present besides Hydrogen, is variable in these models. Detailed specifics of double-degenerate modeling is presented in Section 4.2. Both the SD and DD scenarios are generated via hydrodynamical computer simulations as shown in Figures 1.3 & 1.4. While each of the models are accepted theoretical predictions, the direct telescopic detection of the progenitor system is difficult, with most DD models leaving no post-explosion indication of the system responsible. There have, however, been recent constraints placed on the direct detection of progenitor systems following SD models [32; 33]. Fortunately, other methods of progenitor system constraint come from the unique modeling of these explosions by Röpke et al. (2012) and Seitenzahl et al. (2013), all of which are verifiable via the study of radioactive decay in late-time bolometric light curves (apparent magnitude with respect to time) of SNe Ia [27; 34].

1.3 Light Curves of SNe Ia

By Arnett’s Law, the total electromagnetic light, known as bolometric luminosity, produced at peak magnitude is proportional to the rate of energy deposition by the radioactive decay chain $^{56}\text{Ni} \xrightarrow{t_{1/2}=6.08\text{ d}} ^{56}\text{Co} \xrightarrow{t_{1/2}=77.2\text{ d}} ^{56}\text{Fe}$ [35]. For a uniform density, Arnett’s relation goes as:

$$E_{SN} = M_{Ni}q \quad (1.1)$$

where E_{SN} is the energy of the supernova, M_{Ni} is the total mass of radioactive Nickel produced during explosion, and q is the energy synthesized in the decay chain. While Arnett’s Law is an approximation, the decay of ^{56}Ni remains the most prominent source of heating in SNe Ia and produces primarily γ -rays and positrons, whose energies are deposited and thermalized in the expanding supernova ejecta material [36]. Due to the high opacity of the the expanding ejecta at early times, the optical photons produced in explosion cannot escape immediately. This process of particle escape is critical in defining the shape of the light curve at peak luminosity. The light curve width τ_{LC} can be approximated to be:

$$\tau_{LC} \propto \kappa_{opt}^{1/2} M_{ej}^{3/2} E_K^{-1/4} \quad (1.2)$$

where κ_{opt} is the optical opacity, M_{ej} is the mass of the ejecta, and E_K is the energy of the explosion [35]. After peak luminosity, at later times in the light curve evolution, the ejecta becomes optically thin. This allows for particle escape and the possibility of free streaming γ -rays. However, the fraction of particles trapped in the ejecta compared to those that escape are specific to a given SNe Ia explosion. These processes are discussed at greater length in Section 3.2 and applied in the analysis of SN 2013aa.

Not only can the total mass of ^{56}Ni be determined from the peak luminosity, the abundances of isotopes generated in decay chains $^{57}\text{Co} \rightarrow ^{57}\text{Fe}$ and $^{55}\text{Fe} \rightarrow ^{55}\text{Mn}$ can be indirectly detected from the light curve evolution of SNe Ia at epochs > 300 days after explosion [37]. The procedure for calculating the masses of ^{56}Co , ^{57}Co , and ^{55}Fe produced in SN Ia involves fitting the light curve with a multi-variable decay law known as the Bateman Equation (See Section 3). Model analysis has shown that the mass ratios of these nucleosynthetic yields such as $M(^{57}\text{Co})/M(^{56}\text{Co})$ differ between single and double degenerate explosion models, thus making them extremely useful in identifying the pre-explosion SNe Ia progenitor systems [27].

1.4 Late-time Studies of SNe Ia

Testing each explosion model requires precise photometric data from continuous observations of nearby SNe Ia > 400 days after peak luminosity. This is a challenging effort due to the variability of SNe Ia explosions coupled with the ability to perform accurate photometric measurements at late enough epochs to detect the radioactive decay of isotopes other than ^{56}Ni . Nonetheless, a few significant studies have been recently performed on SNe Ia in close proximity to us and with multiple broad band photometric detections produced at late epochs.

Supernova SN 2011fe remains to be one of the most highly studied late-time SNe Ia, with numerous examinations of radioactive decay channels since its nearby discovery [38]. Shappee et. al (2017) were able to detect abundances of ^{56}Co and ^{57}Co as well as place an upper limit on the mass of ^{55}Fe , while indicating that the fits to the data preferred a DD explosion model [39]. A similar

study by Dimitriadis et al. (2017) examined the near infrared (10000-50000 Å) contribution to the bolometric luminosity of SN 2011fe, but found a contradicting alignment to the single-degenerate explosion model of a high central density white dwarf star [40].

Further examinations of extremely late-time supernovae also make predictions of the pre-explosion progenitor system. Graur et al. (2016) finds a distinct detection of ^{57}Co in the light curve of SN 2012cg and predicts a single-degenerate explosion mechanism [41]. The analysis of SN 2014J makes similar conclusions in their determination of mass ratios that prefer a high central density explosion model [42]. Alternatively, the mass ratio found in SN 2015F by Graur et al. (2017) indicates a double degenerate merger of two white dwarfs [43]. Graur et al. (2017) also examines the relationship between the calculated light curve stretch (how broad a light curve is) and $^{57}\text{Co}/^{56}\text{Co}$ in all four late-time SNe Ia, the implications of which we will discuss as it relates to SN 2013aa [43].

The detection of SN 2013aa at a phase of ~ 1500 days after explosion presents a unique opportunity to examine the nucleosynthetic yields of late-time decay. SN 2013aa is the fifth SNe Ia to be observed at an epoch > 1000 days, with a photometric detection at the second latest phase next to SN 2011fe. The measured late-time bolometric luminosity, combined with early-time data, allows for a fitted calculation of radionuclide abundances powering the light curve. The mass ratios of ^{56}Co , ^{57}Co , and ^{55}Fe found in SN 2013aa can then be compared with explosion models as an indicator of the progenitor system. With only four recorded late-time SNe Ia prior to SN 2013aa, this analysis will contribute to the understanding of late-time trends in the light curves of SNe Ia.

In Chapter 2 we present observations and data reduction of SN 2013aa. In Chapter 3 we discuss the calculation of radioactive isotope abundances. In Chapter 4 we examine the implications of measured mass ratios in the context of explosion models and other late-time studies.

2 Observations

In this section, we briefly introduce SN 2013aa, presenting the published photometric and spectroscopic data and basic parameters from early-time data. We also present late-time *Hubble Space Telescope* photometry.

2.1 Early-time Data (up to 400 days)

SN 2013aa was discovered by the Backyard Observatory Supernova Survey (BOSS) on 2013 February 13 [44] and confirmed to be a SN Ia on 2013 February 16 via its spectral features [45]. SN 2013aa is located in the barred spiral galaxy NGC 5643, 74'' West and 180'' South from the galactic center [46]. Another SN Ia, SN 2017cbv, is in the same galaxy, providing an independent distance estimate to SN 2013aa (Shappee et al., in preparation). Applying the SALT2 algorithm [47] to the SN 2017cbv data, we determine that the distance to NGC 5643 is 13.95 ± 0.35 Mpc, corresponding to a distance modulus of $\mu = 30.72 \pm 0.05$ mag. Primary parameters of SN 2013aa and its host galaxy, NGC 5643, are reported in Table 2.1. Explosion imaging presented in Figure 2.1

SN 2013aa was initially followed by the Las Cumbres Observatory Global Telescope (LCOGT) Supernova Key Project [48], with the light curves including *BVgri* bandpass filters [46]. As mentioned in Graham et al. (2017) [46], most of the near-peak photometry was saturated, thus we complement the early-time light curve with optical (*UBV* telescope filters) data from the *Swift* Optical/Ultraviolet Supernova Archive [SOUSA; 49]. This data provides adequate coverage of the SN from -10 to ~ 200 days after peak. Additionally, Graham et al. (2017) [46] present *gri* filter pho-

Table 2.1: Main Parameters of SN 2013aa and Host Galaxy

Host Galaxy	NGC 5643
Galaxy Type	SAB(rs)c
Redshift	0.003999 ± 0.000007
Distance	13.95 ± 0.3 Mpc
Distance Modulus, μ	30.72 ± 0.05 mag
RA _{SN}	$14^{\text{h}}32^{\text{m}}33.919^{\text{s}}$
Dec _{SN}	$-44^{\circ}13'28.763''$
Stretch	1.072 ± 0.014
m_B^{peak}	11.11 ± 0.05 mag
M_B^{peak}	-19.49 ± 0.07 mag

tometry from the Gemini Multi-Object Spectrograph [GMOS; 50], at ~ 400 days after explosion. In Fig. 2.2, we present the early-time (-15 to 50 days from peak luminosity) light curves of SN 2013aa.

We fit the light curves with Python package SIFTO [51], with which we recover a time of maximum light of $\text{MJD}_{\text{max}} = 56342.69 \pm 0.18$, peak brightness of $m_B^{\text{peak}} = 11.11 \pm 0.05$ mag, peak color of $(B-V)_0 = -0.03 \pm 0.05$ mag and a stretch of $s = 1.072 \pm 0.014$. Restricting our fit to only the *Swift* photometry, which covers the peak of the light curve, we calculate $s = 1.067 \pm 0.023$, consistent with what was found using all available data. Adopting the distance modulus from SN 2017cbv, $\mu = 30.72 \pm 0.05$ mag, SN 2013aa had a *B*-band absolute magnitude at peak of $M_B^{\text{peak}} = -19.49 \pm 0.07$ mag. The relatively high peak absolute magnitude is consistent with its slightly broad light curves. A collection of SN 2013aa spectra is presented in Fig. 2.2, spanning from 32 to 398 days after peak. These spectra have been published by Childress et al. (2015) and Graham et al. (2017) [46; 52]. All the spectra were retrieved through the WISeREP archive ¹ [53].

¹<http://wiserep.weizmann.ac.il/>

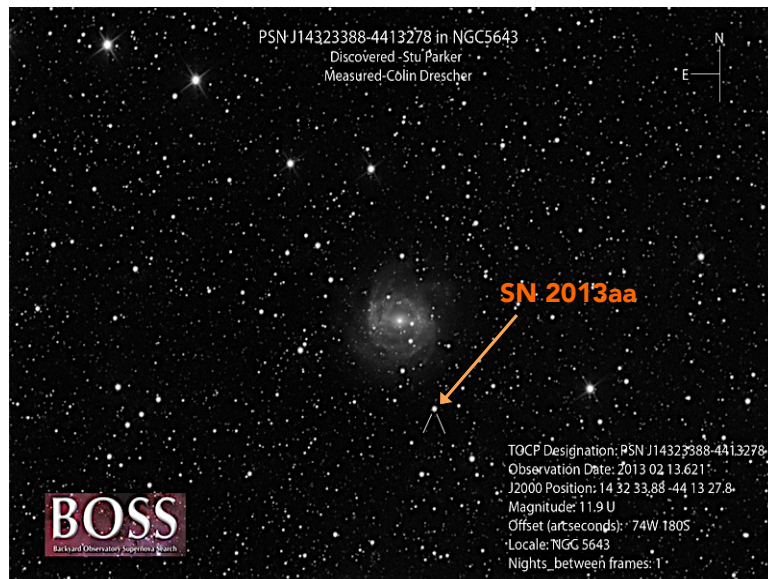


Figure 2.1: Explosion imaging of SN 2013aa in galaxy NGC 5643 on 13 February 2013 by the Backyard Observatory Supernova Search (BOSS) [44].

We used the Supernova Identification package [SNID; 54] and Superfit [55] at the earliest spectrum (32.3 days after peak) to sub-classify SN 2013aa. Both packages reported SN 1991T-like objects as having the best-matching spectra in accordance with the early-time light-curve evolution. However, SN 1991T-like objects are difficult to distinguish from lower-luminosity SNe Ia a month after peak, and thus the sub-classification is somewhat uncertain. With this in mind, throughout this paper, we will consider SN 2013aa as a normal-to-overluminous SNe Ia.

2.2 Hubble Space Telescope (HST) Data

Due to its distance and significant offset from its host galaxy, SN 2013aa is an excellent target for late-time observations. Under *HST* program DD-14925 [56], we imaged SN 2013aa ($\alpha = 14^{\text{h}}32^{\text{m}}33.919^{\text{s}}$, $\delta = -44^{\circ}13'28.763''$) on 2017 March 22, 24, 26 & 30 with the *HST* Wide Field Camera 3 (WFC3). These observations were obtained in parallel with STIS observations of SN 2017cbv. The source was observed with wide-band filters *F350LP* (3000-10000 Å), *F555W*

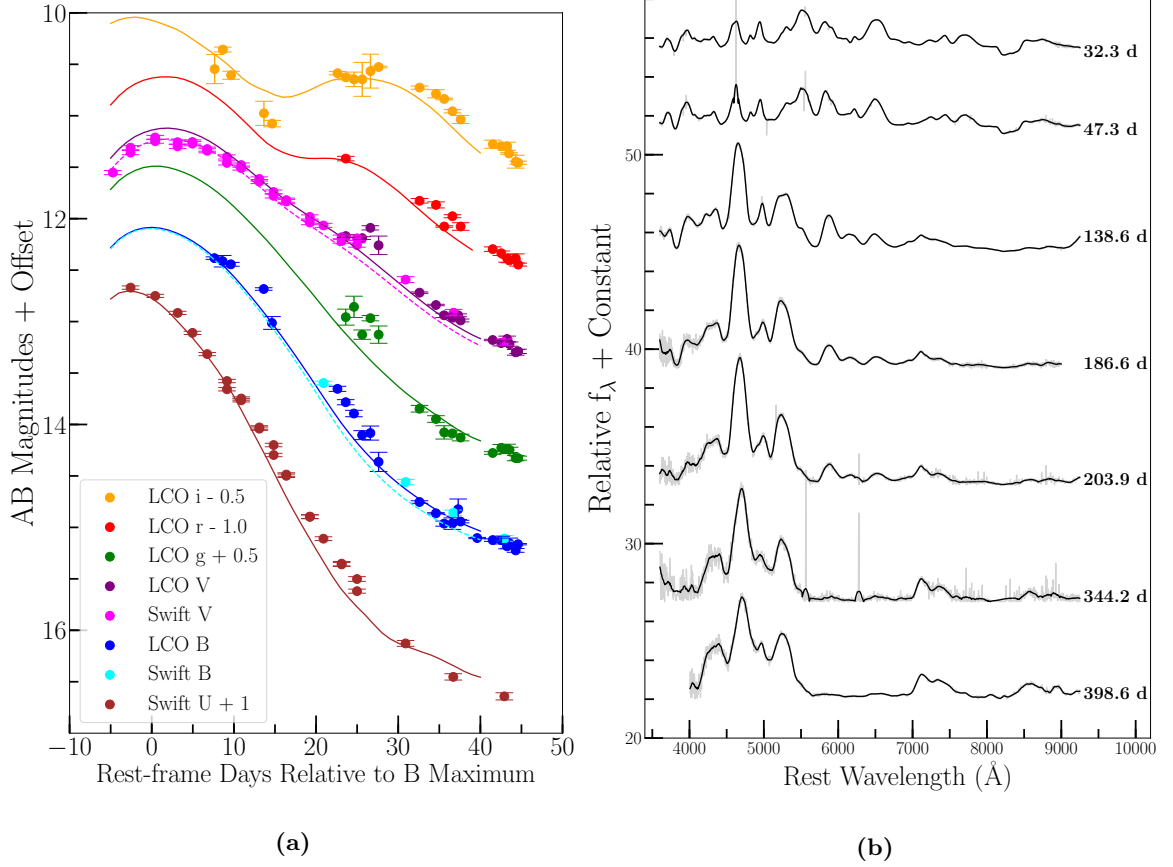


Figure 2.2: LCOGT and Swift light curves of SN 2013aa around peak. LCOGT photometry in shown as B (blue), V (purple), g (green), r (red) and i (orange). Swift photometry shown as U (brown), B (cyan) and V (magenta). The photometry has been corrected for MW extinction. Solid and dashed lines are the SIFTO fits on the LCOGT and Swift photometry respectively. (b) Spectra of SN 2013aa. Raw spectra are shown in gray, smoothed spectra with black lines.

Table 2. Photometric Observations

MJD	Band	Exp. Time (s)	AB Mag ^a	Telescope
57834 - 57842	350LP	507 - 537	27.969 (0.082)	<i>HST</i> /WFC3
57834 - 57842	555W	507-537	27.971 (0.280)	<i>HST</i> /WFC3
57834 - 57842	814W	1014-1074	27.465 (0.177)	<i>HST</i> /WFC3

^a1- σ uncertainties in parentheses.

Note. — Exposures were taken on 2017 March 22, 24, 26, and 30. All four days of observations were combined into a single image for each respective filter.

(4300-7000 Å), and *F814W* (7000-9700 Å) at varying exposures times. Photometric measurements are reported in Table 2.

We received *HST* WFC3 image files in the FLC format, all of which have been corrected for dark current, flat fielding, and charge transfer efficiency through the *HST* calibration pipeline. We used the IRAF package *StarFind* to located reference stars for initial frame alignment. We performed fine alignment of all images to one-another using calibration algorithm TWEAKREG. With all frames aligned, we ran the ASTRODRIZZLE reduction package [57] for cosmic ray removal and generation of median and drizzled science images for each *HST* filter used. We constructed a drizzled template image of all *HST* filters by overlaying each frame, which was then used as reference during photometric calculations.

To determine the position of SN 2013aa in the WFC images, we performed a geometric transformation between the *HST* images and Gemini images taken when the SN was brighter. Using 21 stars common to each image and the Gaia stellar catalog, we calculated a position for SN 2013aa

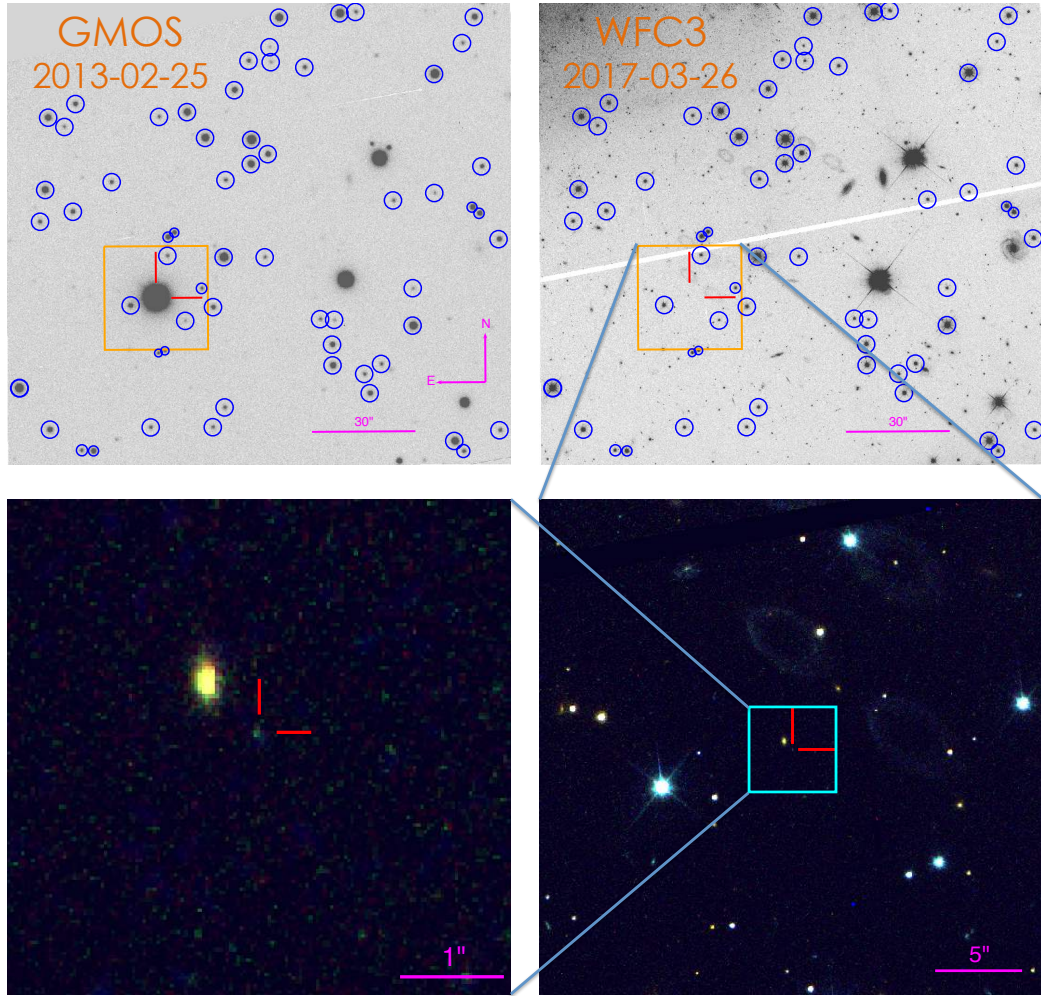


Figure 2.3: *Top Images:* Explosion image taken by *Gemini* with GMOS (left). *HST* image of SN 2013aa at 1500 day epoch taken with WFC3. Stars used for astrometric solution circled in blue. *Bottom Images:* *HST* RGB images centered on SN 2013aa with 30'' (right) and 5'' (left) radii from the source.

in the World Coordinate System (WCS) for both *HST* and *Gemini* images. We aligned the WCS of the *HST* image to that of *Gemini* based on 72 common, unsaturated stars. We then determined the position of SN 2013aa in the *HST* images.

We determined the positional systematic uncertainty related to our geometric transforma-

tion by performing the transformation many times using a bootstrap resampling (with replacement). This involved calculating the coordinates of SN 2013aa using a variety of different standard stars and applying each WCS solution in order to find a total uncertainty on the final coordinate position. The final positional uncertainty is a combination of the systematic uncertainty, the statistical uncertainty of the geometric transformation, and the statistical uncertainty from centroiding the SN.

Our best estimate of the position of SN 2013aa is $\alpha = 14^{\text{h}}32^{\text{m}}33.919^{\text{s}} \pm 0.003^{\text{s}}$, $\delta = -44^{\circ}13'28.76'' \pm 0.03''$. Images of SN 2013aa with reference stars are displayed in Figure 2.3. We detected a point source in our *HST* image that was $+0.01''$ East and $+0.01''$ North of the supernova position found in the Gemini explosion image. This translates to a 0.31σ offset in Right Ascension and a 0.33σ offset in Declination. The position of the sources in both *HST* and Gemini images agree with one another, which suggests that they are in fact the same source.

We performed Point Spread Function (PSF) photometry with photometry package DOLPHOT [58] on the *F350LP*, *F555W*, and *F814W* images. This package calculates apparent magnitudes and uncertainties for every star-like light source in a given image file. DOLPHOT ran simultaneously on all frames while using the combined template *HST* frame for reference. We used default WFC3 DOLPHOT parameters in the input file, keeping the sigPSF value (minimum signal-to-noise for a PSF calculation) at 10. Using 52 PSF stars in the photometric solution, we detected a point source in all three filter frames that was within the uncertainties of the astrometric solution, confirming that this was indeed SN 2013aa. The source is shown most clearly in the bottom panel of Figure 2.3.

In this DOLPHOT detection, we measure the apparent magnitudes of SN 2013aa to be 27.969 ± 0.082 in *F350LP*, 27.971 ± 0.280 in *F555W*, and 27.465 ± 0.177 in *F814W*, corresponding to signal-to-noise ratios of 13.3, 3.9, and 6.1, respectively. The brightness of this source is similar to that expected for a SN 2013aa at this epoch. We calibrated our apparent magnitudes from DOLPHOT to AB magnitudes using the WFC3/UVIS2 photometry zeropoint tables given by the Space Telescope

Science Institute (STSci) ². As a result of the default aperture correction performed by DOLPHOT during the photometry calculation process, we applied the infinite aperture zeropoint values to our generated absolute magnitudes.

To determine the chance coincidence between SN 2013aa and our identified source (i.e., the statistical uncertainty that we had identified a point source other than SN 2013aa), we look at other detected objects within a 5'' radius of SN 2013aa. We limit the sample of reasonable objects to have $S/N \geq 5$, be classified as a star by DOLPHOT (type 1 or 2), have a roundness of < 0.5 (as determined by DOLPHOT), have a sharpness between -0.3 and 0.3 , and have a DOLPHOT photometric quality flag of 0 or 1. We find 10 reasonable objects with a 5'' radius, resulting in a chance coincidence of only 0.2%.

²<http://www.stsci.edu/hst/wfc3/>

3 Analysis

In this section we detail how we generated a pseudo-bolometric light curve from the photometric data described in Section 2. We then discuss our analysis of different elemental decay chains responsible for light curve shape and the process of determining each radioactive isotope mass based on the fit to our bolometric luminosity data.

3.1 Constructing a Pseudo-Bolometric Light Curve

Due to the fact that all data collected was in the optical range (3000-10000Å), we are unable to estimate the total electromagnetic luminosities (bolometric luminosity) at a given epoch. Thus, we created a pseudo-bolometric light curve with our best estimates for the total light produced at certain dates of observation. In order to construct the pseudo-bolometric light curve of SN 2013aa, we employ similar techniques as performed for other late-time SN Ia studies. This includes the modification of the SN spectra to match a series of photometric observations and, subsequently, integration of these modified spectra over the optical wavelengths [e.g., 39; 40; 41; 43; 59]. We correct all photometric data, both ground- and space based, for Milky Way Extinction according to Cardelli et al. (1989) with $R_v = 3.1$, and find no host-galaxy extinction to correct for in the data [60].

For photometric epochs with phases of ~ 100 to 200 days, we modify the closest-in-time spectrum to match that of the LCOGT photometric data using a process called spectroscopic mangling [61]. For the ~ 400 -day epoch, we perform the same operation with the GMOS photometry

and spectrum. For the 1500-day photometric epoch, there is no spectrum of SN 2013aa or any other SN Ia so we instead use a 1000-day spectrum of SN 2011fe [62]. The bolometric flux is computed by integrating each modified synthetic spectrum from 4000–9000 Å and obtaining errors by Monte Carlo resampling of the observed photometry. Finally, we calculate the optical bolometric luminosity by scaling the integrated flux with the distance to the SN, estimated in Section 2.1.

The choice of wavelength range for generating the pseudo-bolometric light curve was set by the wavelength coverage of the available spectra, and in particular the GMOS spectrum (see Fig. 2.2). While this wavelength range is narrower than pseudo-bolometric light curves generated for other SNe Ia (usually ~ 3500 – 10000 Å), the dominant spectral lines of SNe Ia at these phases, mainly from iron peak elements and Ca II, are included in our wavelength range. We can estimate the fraction of flux lost bluewards (3500–4000 Å) and redwards (9000–10000 Å) of our pseudo-bolometric wavelength range by using spectra of the well-observed SN 2011fe: we calculate a fraction of 5% and 9% at 348d, reducing to 4% and 7% at 1034d. Our closest spectrum to the GMOS spectrum at 398d is the WiFeS spectrum at 344d, which spans from 3500–9280Å, for which we estimate a fraction of flux lost bluewards (i.e. the integrated flux from 3500–4000 over the integrated flux from 3500–9280Å) and redwards (i.e. the integrated flux from 9000–9280 over the integrated flux from 3500–9280Å) of our pseudo-bolometric wavelength range to be 1.2% and 1.5% respectively. By using spectra of the well-observed SN 2011fe, which cover a wider wavelength range (3000–10000Å), the equivalent blueward-redward flux losses are 5% and 9% at 348, reducing to 4% and 7% at 1034d.

3.2 The Bolometric Light Curve Model

The light curve of a SN Ia is powered by the thermalization of the expanding ejecta due to the deposition of energy from the radioactive decay of several decay chains. At early times, the dominant contribution comes from ^{56}Ni , the most abundant synthesized element, and its daughter isotope, ^{56}Co , with its decay channel $^{56}\text{Co} \xrightarrow{t_{1/2}=77.2\text{d}} ^{56}\text{Fe}$ being the most important for epochs up to 2 yrs after explosion. At later times, and as the column density of the expanding ejecta

decreases, additional energy is deposited by the radioactive decays of $^{57}\text{Co} \xrightarrow{t_{1/2}=271.2\text{ d}} ^{57}\text{Fe}$ and $^{55}\text{Fe} \xrightarrow{t_{1/2}=999.67\text{ d}} ^{55}\text{Mn}$. All of these decay chains produce γ -rays, X-rays and charged leptons (positrons, Auger electrons, and internal conversion electrons). In our analysis we employ the decay energies and constants presented in Table 3. In this framework, the luminosity produced can be approximated by the Bateman equation:

$$L_A(t) = 2.221 \frac{\lambda_A}{A} \frac{M(A)}{M_\odot} \frac{q_A^x + q_A^l f_A^l(t) + q_A^\gamma f_A^\gamma(t)}{\text{keV}} \exp(-\lambda_A t) \times 10^{43} \text{ erg s}^{-1} \quad (3.1)$$

where t is time since explosion, λ_A is the decay constant, A is the atomic number, and q^l , q^γ , and q^x are the average energies of charged leptons, γ -rays, and X-rays, respectively, per decay. In this equation, $f_A^\gamma(t)$ and $f_A^l(t)$ describe the trapping of the deposited energy of the γ -rays and charged leptons respectively, and, assuming homologous expansion, are given by

$$f_A^{\gamma,l} = 1 - \exp\left[-\left(\frac{t^{\gamma,l}}{t}\right)^2\right] \quad (3.2)$$

In previous late-time studies, such as Graur et al. (2016), Shappee et al. (2017), and Graur et al. (2017), with late-time data > 500 days, the authors consider only the charged leptons deposited energy, for which they assume complete trapping in the decay of ^{56}Co (e.g., $f_A^l = 1$), and no positron trapping in the decays of ^{57}Co and ^{55}Fe (e.g., $f_A^l = 0$). [39; 41; 43]. For the ^{56}Co γ -rays, a timescale of $t_{56}^\gamma \approx 35$ days was found to fit the late-time light curves of several SNe Ia [63; 64; 65]. While these SNe Ia do have lower predicted mass of ^{56}Ni than SN 2013aa, the application of $t_{56}^\gamma \approx 35$ days is still an adequate assumption and has no effect on the analysis.

While Equation 3.1 describes the *bolometric* luminosity (that is, the complete energetic output across the electromagnetic spectrum), the photometric data presented here and in (most of) the aforementioned studies are primarily optical data, with some cases including near-infrared observations. A common approach is to assume that the *optical* luminosity scales with the complete bolometric one as $L_{\text{opt}}(t) = B(t) \times L_{\text{bol}}(t)$, where $B(t)$ is the fraction of the bolometric luminosity in the optical and is often assumed to be a constant in time. In this sense, $1/B(t)$ resembles a

Table 3. Energies Per Decay and Radioactive
Decay Constants

Nucleus	λ_A (s ⁻¹)	q^l (keV)	q^γ (keV)	q^x (keV)
⁵⁶ Co	8.975e-3	124.61	3606	1.587
⁵⁷ Co	2.551e-3	17.82	121.6	3.6
⁵⁵ Fe	6.916e-4	3.973	-	1.635

“bolometric correction”, i.e. a function that transforms the optical flux to a bolometric one. We can estimate $B(t)$ by calculating the ratio between the ⁵⁶Co mass found by fitting the late-time data with Equation 3.1 over the total ⁵⁶Ni mass as determined from data around peak (where ⁵⁶Ni dominates), for which the non-optical contribution at this phase is $\leq 15\%$ [e.g. see 66, for SN 2011fe]. Values of $B(t)$ calculated by Graur et al. (2017) for a sample of SNe Ia with late-time data range from 20-40%. However, Dimitriadis et al. (2017) showed that, for SN 2011fe, a non-constant B can explain the increase of the late-time non-optical contribution, approximating the optical contribution with a sigmoid function:

$$B(t) = 1 - \frac{P_0}{1 - e^{P_1 \times (t - P_2)}} \quad (3.3)$$

In that work, this non-optical contribution, consisting of the *JHK* near-infrared bands, increases from ~ 5 to 35%, from 200 to 600 days after the *B*-band maximum brightness. This effect can be seen as a faster decline of the (optical bolometric) light curve at these epochs, compared to the expected radioactive decay slope, predicted by known radioactive decay chains. The physical origin of this faster decline remains elusive: positron escape models, a re-distribution of optical flux to the mid/far-infrared [67] or time-dependent effects, such as freeze-out could provide an explanation.

3.3 Results from Light-Curve Model Fitting

In this work, we will explore four models for the late-time light curve of SN 2013aa: (1) Complete positron trapping (e.g., $f_A^l = 1$ & negligible $t_{55,56,57}^l$) and free-streaming γ -rays at late-times (e.g., $f_{55,57}^\gamma = 0$ & negligible $t_{55,57}^\gamma$), (2) the same as 1, but with possible positron escape, for which we will assume a same form of f_A^l as the trapping function of the γ -rays (e.g., as in Equation 3.2), (3) the same as 1, but with a time-dependent non-optical contribution (Equation 3.3), and (4) the same as 1, but with no ^{55}Fe , as was assumed by Graur et al. (2017). For all of our fits, we assume $t_{56}^\gamma = 35$ days, and, by applying a Markov-Chain Monte-Carlo fitting algorithm, determine the amount of ^{56}Co , ^{57}Co , and ^{55}Fe . In our analysis, we use *emcee*, a Python-based application of an affine invariant Markov-Chain Monte Carlo (MCMC) with an ensemble sampler [68]. Working with an MCMC allows for the detection of degeneracy amongst free variables that could not be properly identified with a standard χ^2 fitting algorithm. Unfortunately, SN 2013aa has no data between 400 and 1500 days. As a result, it is difficult to separate the contributions of ^{57}Co and ^{55}Fe to the late-time light curve. However, the current data are still constraining for explosion models.

An important step in consistently comparing our late-time mass estimates of the different scenarios considered, is an accurate determination of the total ^{56}Ni mass, synthesized in the explosion. At early times, the luminosity is dominated by the ^{56}Ni decay and almost all of the light is emitted in the optical [e.g., 66]. In the sample study of Graur et al. (2017), the authors estimate the ^{56}Ni mass by fitting a straight line to the M_{56} values of Childress et al. (2015) over their SIFTO stretch values [52]. A similar calculation for SN 2013aa yields $M_{56} = 0.732 \pm 0.151 M_\odot$. As a consistency check, we additionally estimate the ^{56}Ni mass from the bolometric luminosity at peak, following the widely-used Arnett law [35]. Using our early-time photometry (Section 2.1) and a template SN Ia spectrum from Hsiao et al. (2007) at peak [61], we integrate the spectrum and estimate a peak luminosity of $L_{peak} = 1.56 \pm 0.05 \times 10^{43} \text{ erg s}^{-1}$. Assuming a rise time of 17 days, we estimate $M_{56} = 0.73 \pm 0.03 M_\odot$. In the following sections, we will follow the Graur et al. (2017)

approach and adopt $M_{56} = 0.732 \pm 0.151 M_{\odot}$.

In Fit 1, we considered complete positron trapping and a fixed $t_{56}^{\gamma} = 35$ days in fitting for the masses of ^{56}Co , ^{57}Co , and ^{55}Fe . We find a ^{56}Co mass of $0.589_{-0.0140}^{+0.0140} M_{\odot}$, which is 20% less than the total mass of ^{56}Ni calculated from the near-peak data. Additionally, we find estimates of ^{57}Co and ^{55}Fe masses of $M(^{57}\text{Co}) = 2 \times 10^{-5+1 \times 10^{-4}}_{-2 \times 10^{-5}} M_{\odot}$, and $M(^{55}\text{Fe}) = 0.006_{-0.006}^{+0.001} M_{\odot}$. This fit yields a $\chi^2/\text{dof} = 298.4/23$, and we calculate a mass ratio of $^{57}\text{Co}/^{56}\text{Co} = 3 \times 10^{-5+2 \times 10^{-4}}_{-3 \times 10^{-5}}$. For this scenario, the best-fitting values have significantly more ^{55}Fe than ^{57}Co , although the range of allowed values include having the mass hierarchy inverted. Unlike the other fits displayed in Figure 3.1, Fit 1 is significantly more luminous at 400 days than the data, suggesting that – under the assumption of a constant bolometric correction – incomplete positron trapping occurs at 400 days, and is therefore likely to also occur at later times.

In Fit 2, we fit for all three radioactive isotope masses in addition to t_{56}^l , which allows for positron leakage (see Equation 3.2). This varies from Fit 1 in that we now consider only partial positron trapping as well as a fixed $t_{56}^{\gamma} = 35$ days. The ^{56}Co , ^{57}Co , and ^{55}Fe masses are estimated to be $0.631_{-0.0150}^{+0.0150} M_{\odot}$, $0.006_{-0.006}^{+0.001} M_{\odot}$, and $0.0002_{-0.0002}^{+0.0007} M_{\odot}$, respectively. We find that the best-fitting value of ^{56}Co is 14% less than the near-peak estimate of ^{56}Ni , and we calculate a mass ratio $^{57}\text{Co}/^{56}\text{Co} = 0.01_{-0.01}^{+0.002}$. This model has a $\chi^2/\text{dof} = 20.4/22$. Fit 2 is much better at matching the data near 400 days than Fit 1. We find that fitting for partial rather than complete positron trapping yields a timescale of $t_{56}^l = 281.02_{-15.290}^{+16.440}$ days for lepton escape.

In Fit 3, we fit for ^{57}Co , ^{55}Fe , and each free parameter of the sigmoid function in Equation 3.3, while fixing the mass of ^{56}Co to the value determined from the early-time data, $M_{56} = 0.732 \pm 0.151 M_{\odot}$. Similar to Fit 1, this model includes complete positron trapping, but with an increasing non-optical contribution to the total luminosity of the light curve. We measure the ^{57}Co mass to be $0.015_{-0.015}^{+0.0075} M_{\odot}$, and a mass ratio $^{57}\text{Co}/^{56}\text{Co} = 0.02_{-0.02}^{+0.01}$. The best-fitting value for the mass of ^{55}Fe is only $7 \times 10^{-7+7 \times 10^{-6}}_{-7 \times 10^{-7}} M_{\odot}$, significantly smaller than the best-fitting values of the other fits, but consistent with their range for the ^{55}Fe mass. This fit has a $\chi^2/\text{dof} = 21.3/20$ and,

Table 4. Model Fit to Pseudo-Bolometric Light Curve Data

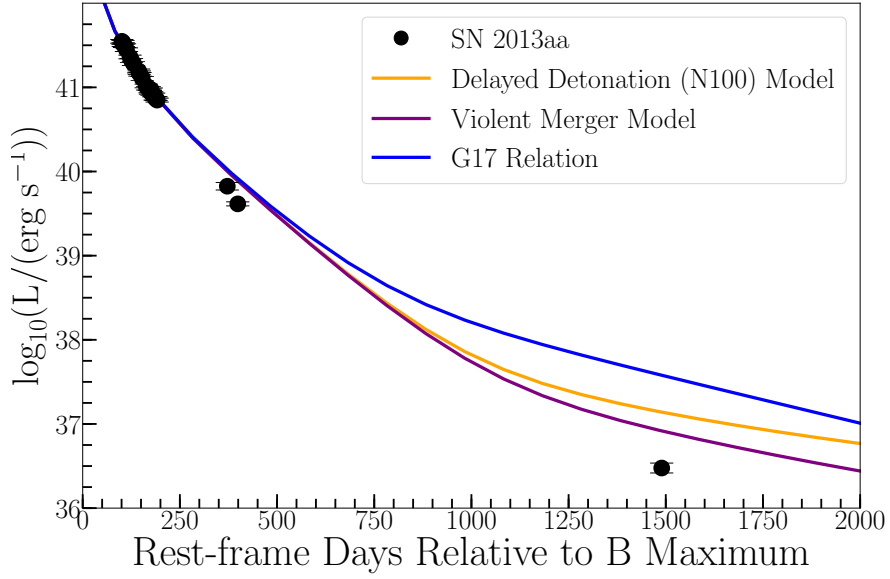
Model	^{56}Co (M_{\odot})	^{57}Co (M_{\odot})	^{55}Fe (M_{\odot})	t_{56}^{γ}	t_{56}^l	χ^2	DOF
Fit 1	$0.589_{-0.014}^{+0.014}$	$0.00002_{-0.00002}^{+0.0001}$	$0.006_{-0.006}^{+0.001}$	35^a	-	298.4	23
Fit 2	$0.631_{-0.015}^{+0.015}$	$0.006_{-0.006}^{+0.001}$	$0.0002_{-0.0002}^{+0.0007}$	35^a	$281.02_{-15.29}^{+16.44}$	20.4	22
Fit 3	0.732^a	$0.015_{-0.015}^{+0.0075}$	$0.0000007_{-0.0000007}^{+0.0000007}$	35^a	-	21.3	20
Fit 4	$0.59_{-0.01}^{+0.01}$	$0.006_{-0.001}^{+0.001}$	0^a	35^a	-	299.7	24

^aFixed during fitting.

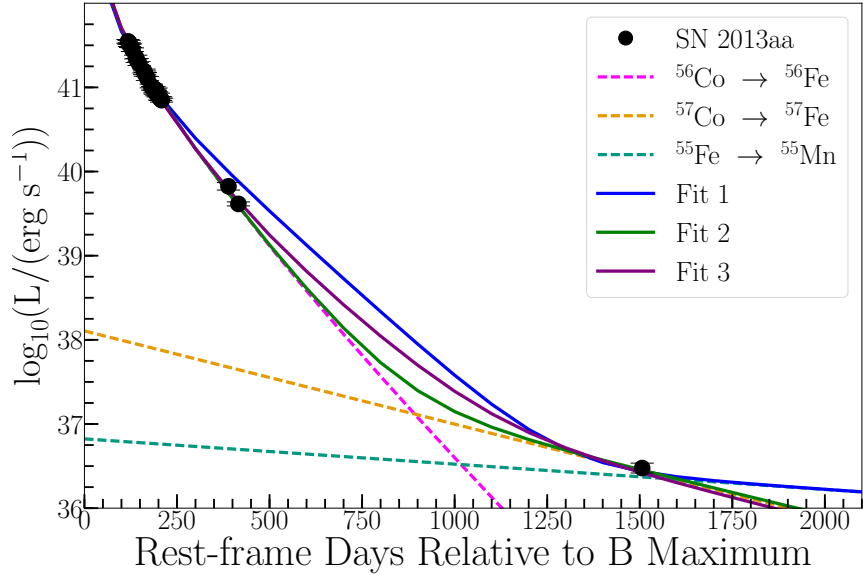
like Fit 2, matches the data at 400 days 3.1.

Finally for Fit 4, we set the ^{55}Fe mass to be zero. This is done to be consistent with the Graur et al. (2017) analysis [43]. We find ^{56}Co and ^{57}Co masses of $0.59_{-0.010}^{+0.010} M_{\odot}$ and $0.006_{-0.001}^{+0.001} M_{\odot}$, respectively. The best-fitting value of ^{56}Co is 20% less than the total the near-peak estimate of ^{56}Ni , and we calculate a mass ratio $^{57}\text{Co}/^{56}\text{Co} = 0.01_{-0.002}^{+0.002}$. This fit has a $\chi^2/\text{dof} = 299.7/24$ and, like Fit 1, is over-luminous, relative to the data, around 400 days after peak brightness. Although Fit 4 is not a particularly good representation of the data, we use the mass ratios measured here when comparing to other SNe Ia examined by Graur et al. (2017) in Section 4.2.

Best-fitting parameters for each model are reported in Table 4, with each respective fit plotted in Figure 3.1.



(a)



(b)

Figure 3.1: (a) Bolometric luminosities of SN 2013aa with respect to SD (orange) and DD (purple) explosion models using fractions of ^{56}Co predicted by Röpke et al. (2012). Blue line is calculated from the expected mass of ^{57}Co based on fit for $^{57}\text{Co} / ^{56}\text{Co}$ versus stretch shown by Graur et al. (2017). This trend is plotted in Figure 4.1. (b) Our three separate fits to bolometric data. Values found for ^{56}Co , ^{57}Co , and ^{55}Fe reported in Table 4. Other three lines represent the decomposition of ^{56}Co , ^{57}Co , and ^{55}Fe decay chains using the masses found in Fit 2 as well as the upper limit of $M(^{55}\text{Fe})$ measured in Fit 1.

4 Discussion

4.1 Comparison to Explosion Models

The mass ratios between given radioactive isotopes are indicators of the explosion mechanism in SNe Ia. We compare our values for $^{57}\text{Co}/^{56}\text{Co}$ with the two explosion models presented in Röpke et al. (2012), both of which probe the two extremes of central density: The ddt_n100 [34], a Delayed Detonation, near-Chandrasekhar mass explosion model, with $\rho_c \sim 3 \times 10^9 \text{ g cm}^{-3}$, and the merger_11+09 [30], a Violent Merger model of 1.1 and 0.9 M_\odot WDs, with $\rho_c \sim 2 \times 10^6 \text{ g cm}^{-3}$. Figure 3.1 illustrates that the Violent Merger model has a 1500-day luminosity that is more similar to that of SN 2013aa than the Delayed Detonation model. However, both models predict a significantly more luminous event than SN 2013aa. Our preferred description of the data (Fit 3) has $^{57}\text{Co}/^{56}\text{Co} = 0.02^{+0.01}_{-0.02}$, which is more than 0.4σ below that of the Violent Merger model ($^{57}\text{Co}/^{56}\text{Co} = 0.0242$) and 1.1σ below that of the Delayed Detonation model ($^{57}\text{Co}/^{56}\text{Co} = 0.0311$). The other scenarios described in Section 3.3 have even smaller ratios of $^{57}\text{Co}/^{56}\text{Co}$.

Despite the best-fitting values being consistent with zero, the parameter space of our model fits provides estimates for the abundances of ^{57}Co and ^{55}Fe at this late-time epoch. Due to the difficulty in detecting ^{55}Fe , other late-time studies have constrained this isotopic abundance based on the ratio of $^{57}\text{Co}/^{55}\text{Fe}$ predicted in SD and DD explosion models such as Röpke et al. (2012), Ohlmann et al. (2014) and Iwamoto et al. (1999) [25; 27; 69]. We, however, find it inconsistent to enforce a ratio of $^{57}\text{Co}/^{55}\text{Fe}$, but not that of $^{57}\text{Co}/^{56}\text{Co}$ in fitting for the abundance of all radioactive

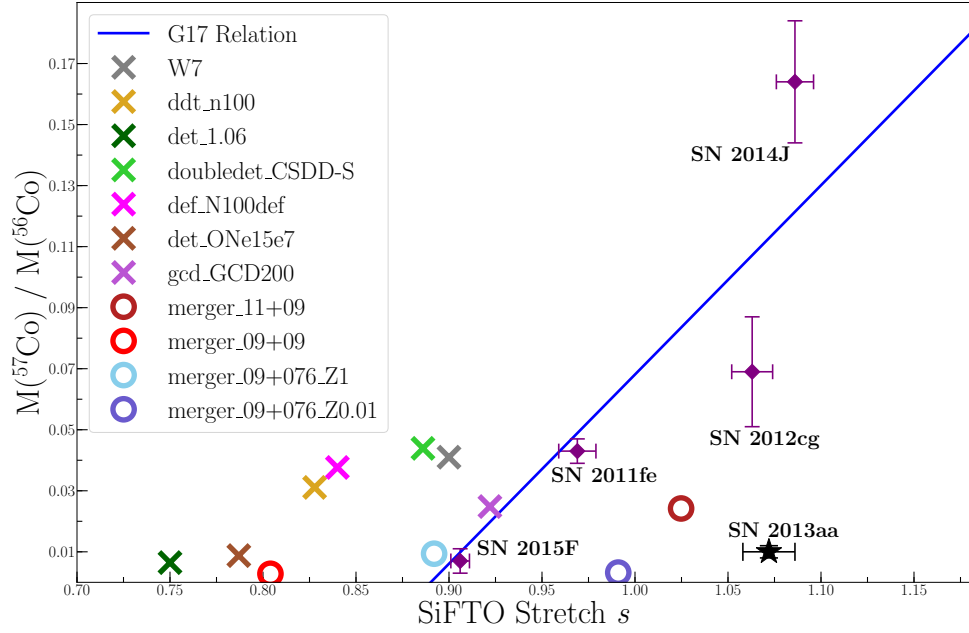
isotopes. In our three fits we choose not to constrain the mass of ^{57}Co nor that of ^{55}Fe , and thus explore the parameter space of each fit without the confinement of an explosion model mass ratio. Nonetheless, the degeneracy between the masses of ^{57}Co and ^{55}Fe cannot be broken by our limited late-time data, and ultimately requires future observation of SN 2013aa in epochs where the presence of ^{55}Fe becomes more prominent in the bolometric light curve.

4.2 Comparison to Other Supernova Observed at Late-Time Epochs

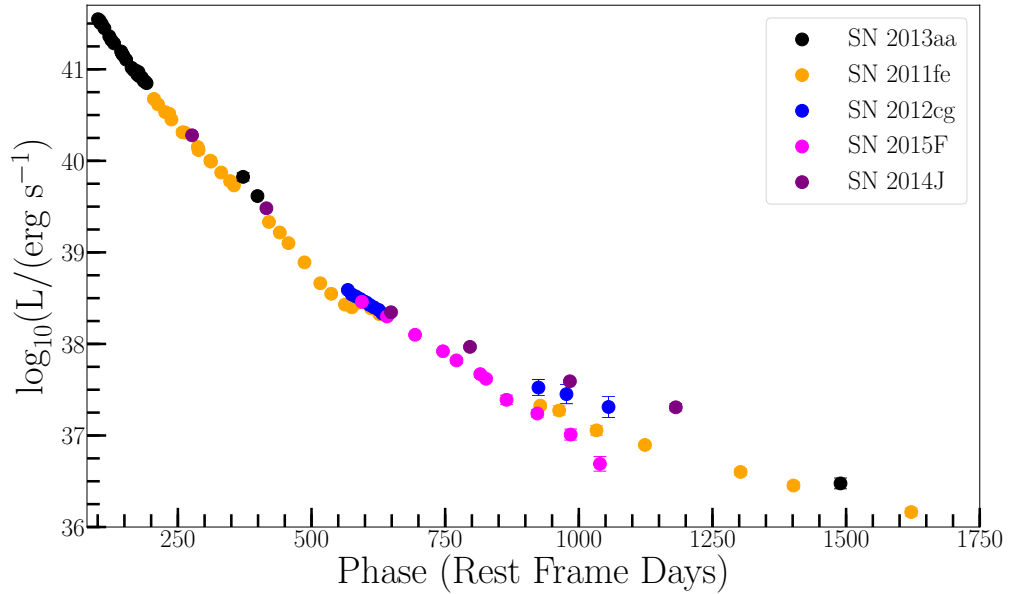
SN 2013aa is the fifth SN Ia used to constrain explosion models via mass ratios of late-time decay elements. Using the four SNe Ia with previous extremely late-time photometry, Graur et al. (2017) found a linear trend between light-curve shape (specifically, SIFTO-calculated stretch values) and $M(^{57}\text{Co})/M(^{56}\text{Co})$. They also found a linear trend between the change in pseudo-bolometric luminosity between 600 and 900 days ($\Delta L_{900} = \log_{10}(L_{600}/L_{900})$) and the time at which freeze-out effects are most prevalent in the light curve, t_{freeze} . We reproduce these trends in Figure 4.1 by fitting a line to the four original data points. In Figure 4.1, we also include the values for SN 2013aa found in Fit 4 (which has the same assumptions as the Graur et al. (2017) analysis). From the figure, we see that SN 2013aa is a large outlier to the Graur et al. (2017) trend.

Using the Graur et al (2017) relation, we estimate a theoretical mass ratio of $M(^{57}\text{Co})/M(^{56}\text{Co})$ corresponding to the stretch value we find for SN 2013aa. We plot that model with respect to bolometric luminosity data as the blue line in Figure 3.1. The Graur et al. (2017) relation predicts a luminosity that is more than an order of magnitude above that of SN 2013aa. We conclude that either SN 2013aa is extremely abnormal or the Graur et al. (2017) relation does not hold for a larger sample.

We also use Figure 4.1 to explore the implication of various explosion models abundances. Apart from the already discussed `ddt_n100`, `merger_11+09` and `W7`, we include models from the



(a)



(b)

Figure 4.1: (a) Reproduction of mass ratio vs. stretch plot from Graur et al. (2017) with added SN 2013aa point. We have displayed the ratios of a variety of single-degenerate and double-degenerate explosion models with their predicted stretch value provided by the Heidelberg Supernova Model Archive. Blue line represents our fit to the Graur et al. (2017) data, excluding SN 2013aa in the fit. (b) Combined pseudo-bolometric light curve data from all late-time SNe Ia studies.

Heidelberg Supernova Model Archive (HESMA)¹ that include various binary configurations and explosion mechanisms. These scenarios are divided based on the progenitor system and explosion mechanism e.g., single-degenerate or double-degenerate. The `det_1.06` [70] is a SD model involving a sub-Chandrasekhar mass detonation of a $1.06 M_{\odot}$ WD, while the `doubledet_CSDD-S` [71] is SD double detonation model of a $0.79 M_{\odot}$ WD (with $M_{CO} = 0.58$ and $M_{He} = 0.21 M_{\odot}$) where the Helium layer detonates in addition to the Carbon-Oxygen layer. We have included the `def_N100def` [72], which is a pure deflagration SD model of involving a $1.4 M_{\odot}$ WD, as well as the `det_ONe15e7` [73], a SD model that has a detonation of a $1.23 M_{\odot}$ O-Ne WD (with homogeneous composition of 3% ^{12}C , 60% ^{16}O and 37% ^{20}Ne). Lastly, for SD models, we have included the `gcd_GCD200` [74], which is a SD model in which a gravitationally confined detonation occurs in a near-Chandrasekhar-mass WD. For comparison, we have also investigated a variety of double-degenerate models in our comparative analysis to late-time SNe Ia. The `merger_09+09` [75] is a violent merger scenario comprised of two $0.9 M_{\odot}$ binary WDs. Lastly, we have included the `merger_09+076_Z1` [76] and the `merger_09+076_Z0.01` [77], which are similar DD models involving 0.76 and $0.9 M_{\odot}$ WDs. The former has solar metallicity while the latter has metallicity $Z = 0.01 Z_{\odot}$. We estimate the stretch of each explosion model by using the equations in Guy et al. (2007) [47] and published Δm_{15} values. This calculation reveals a discrepancy in the fitted relation of Figure 4.1 because, in plotting the predicted mass ratios of each explosion model with respect to specific stretch values, there is no discernible adherence to the trend of other late-time SNe Ia. A brief description of these models and some of their basic physical parameters is presented in Table 5, and more information for each model can be found in the relevant references.

While some late-time SNe are visibly closer in stretch and $M(^{57}\text{Co})/M(^{56}\text{Co})$ values to those of explosion models, i.e. SN 2013aa to the Violent Merger or SN 2015F to the W7 model, there is ultimately no concrete correlation between these specific models and the observed late-time SNe in terms of measured mass ratios and stretch.

¹<https://hesma.h-its.org/doku.php?id=start>

To further understand the late-time luminosity evolution of SNe Ia, we plot the pseudo-bolometric luminosities of all five SNe Ia with extremely late-time data in the right panel of Figure 4.1. Notably, the light curves are very similar through ~ 700 days. After this time, SNe 2012cg and 2014J have higher luminosities than that of SNe 2011fe, 2013aa, and 2015F. In fact, the latter three SNe have nearly identical light curves (up to where their data overlap in time) through 1600 days after explosion. Unsurprisingly, these three SNe have similar isotopic mass ratios, yet there is a noticeable difference between the mass ratio of SN 2013aa and SN 2011fe, despite their similar light curve trend. We conclude that the larger mass ratio found in SN 2011fe is a result of available data in the 500-1000 day phase range in which the relation is presented. The lack of data for SN 2013aa from 500-1000 days after max light, may be the cause of this lower mass ratio.

SNe 2012cg and 2014J, on the other hand, have larger $M(^{57}\text{Co})/M(^{56}\text{Co})$, which has been interpreted as being the result of having near-Chandrasekhar-mass progenitor stars [41; 42]. However, the measured mass ratios is significantly larger than that predicted by the SD models. Moreover, the difference in mass ratios for SNe 2012cg and 2014J is larger than the differences between the different theoretical models. This indicates either systematic effects in the luminosity determination for these SNe, missing physics in the models, or the model parameter space not spanning the physical parameter space.

4.3 Non-Optical Contribution to the Bolometric Luminosity

Since the luminosities calculated for SN 2013aa are confined to the optical band (4000 – 9000 Å), we investigate a non-optical contribution in late-time epochs (particularly at ~ 10000 – 20000 Å). For the case of Fit 1 and 2, the non-optical contribution can be estimated by the ratio of the calculated ^{56}Co to the total ^{56}Ni , for which we find $\sim 20\%$ and $\sim 14\%$, respectively. These values represent the non-optical $B(t)$ term shown in Section 3.2, and the bolometric correction is found by $1/B(t)$. For the case of Fit 3, in which we fit for this non-optical contribution, we examine the sigmoid function with free parameters generated by the MCMC. We find a gradually increasing

non-optical contribution from $\sim 10\%$ at 100d to $\sim 60\%$ after 500d from maximum. These values are broadly consistent with the theoretical prediction of $\sim 20\%$ by Franson et al. (2015) [67]. Moreover, they are consistent with the non-optical contribution estimations of SN 2012cg and SN 2014J based on the Graur et al. (2017) fits.

4.4 Companion Contamination?

In certain cases, the supernova luminosity observed may be affected by a surviving companion star. While we see no visible evidence of companion contamination from the photometric analysis or in the *HST* images, we still consider the potential for a surviving binary companion, which could contribute to the luminosity at late-time epochs. We fit the psuedo-bolometric light curve for the decay of ^{56}Co plus a constant companion luminosity. We calculate a companion contribution to the luminosity of $5.26 \pm 1.04 \times 10^2 L_{\odot}$ with a $\chi^2/\text{dof} = 297.29/24$. Using the mass-luminosity relation [78], this luminosity translates to a main sequence or red giant star with a mass of $\sim 5 M_{\odot}$. In similar studies such as Dimitriadis et al. (2017) and Shappee et al. (2017), an existing companion star was also ruled out based on the lack of pre- and post-explosion detection. We conclude that this scenario is unlikely in the case of SN 2013aa.

4.5 Light Echoes?

During a supernova explosion, some of the light may be reflected off the surrounding interstellar material. This reflected light is known as a light echo and will take longer to arrive at the observer. Due to its late-time arrival, if a light echo did occur, the bolometric luminosity observed in a supernova at later times would not be consistent with its complete light curve evolution, i.e., a dramatic increase in optical light at late-times when exponential dimming should have occurred. Graur et al. (2017) used the late-time SN color evolution to successfully rule out light echo contamination for SN 2015F, by comparing B-V and V-R with the colors of the well-studied SN 2011fe,

which shows no signs of light echo, having exploded in a relatively clean environment. While we cannot repeat the same procedure for SN 2013aa, as we do not have this temporal color information at these phase ranges, we can rule out the presence of a light echo by comparing the SED derived from the *HST* ~ 1500 d photometry with SN 2007af and SN 2011fe: SN 2007af is an otherwise normal SN Ia that showed clear signs of a light echo when observed at ~ 1080 d at the same *HST* photometric bands with SN 2013aa, while for SN 2011fe, we construct a synthetic SED of the *HST* filters, using the Taudenberger et al. (2015) ~ 1035 d spectrum [62].

It is straightforward to rule out light echo contamination, as SN 2013aa is more similar to SN 2011fe: The SED of SN 2007af shows the characteristic blue shape of a light echo spectrum, originating from scattered early-time spectra, which is different for both SN 2013aa and SN 2011fe. The calculated $F555W-F814W$ (similar to V-i) colors are 0.79 ± 0.33 , 0.45 ± 0.02 and -0.49 ± 0.13 for SN 2013aa, SN 2011fe and SN 2007af, respectively.

5 Conclusions

In this paper we have presented *HST* WFC3 imaging of SN 2013aa 1500 days after explosion. Upon detecting the supernova in three optical filters, we determined the respective AB magnitudes to be 27.969 (*F350LP*), 27.971 (*F555W*), and 27.465 (*F814W*). Based on our astrometric solution, we calculate the chance of coincidence for this detection to be 0.2%. Calculated magnitudes at this epoch, combined with photometric data from Swift, LCOGT, and Gemini, allowed for the generation of a pseudo-bolometric light curve.

In our analysis, we applied the Bateman equation in order to fit the radioactive decays of ^{56}Ni , ^{57}Ni , and ^{55}Co to the bolometric luminosities of SN 2013aa. We fit the pseudo-bolometric light curve data with three primary, independent model fits: complete positron trapping (Fit 1), partial positron trapping (Fit 2), and a time-dependent non-optical contribution represented by the sigmoid function (Fit 3). For each model, we estimate the ^{57}Co and ^{55}Fe masses and determine the $^{57}\text{Co}/^{56}\text{Co}$ ratio. For our preferred model (Fit 3), we estimate $^{57}\text{Co}/^{56}\text{Co} = 0.02_{-0.02}^{+0.01}$. This value is more consistent with a low-central density, double-degenerate explosion of two sub-Chandrasekhar-mass white dwarf stars than a high-central density Chandrasekhar-mass single-degenerate WD system.

Compared to other SNe Ia observed at late-time epochs, we find that SN 2013aa does not match the Graur et al. (2017) $M(^{57}\text{Co})/M(^{56}\text{Co})$ vs. stretch trend. However, the relation presented is for a specific phase range of 500-1000 days, during which SN 2013aa has no photometric data. However, the data at ~ 400 and ~ 1500 days is quite constraining in this phase range, and any substantial decrease in luminosity at the 400-500 day or 1000-1500 day phase range is unlikely due

to SN 2013aa’s light curve similarity to other late-time SNe Ia. We explore the possibility that the discrepancy in mass ratios may be caused by a major shift in light, the result of which being a substantial non-optical contribution at late-times [63; 65; 67]. However, if this were the case and SN 2013aa conformed to the predicted mass ratio by Graur et al. (2017), only $\sim 10\%$ of the light at late-times would come from the optical based on our calculated ratio of $M(^{57}\text{Co})/M(^{56}\text{Co})$. While SN 2013aa may be an outlier to the trend of Graur et al. (2017), we cannot sub-classify the target as any different than a normal SN Ia (e.g. 1991T-like) as a result of ambiguity in fitting spectral features.

We note that SN 2013aa’s light-curve evolution and its isotopic mass ratio are similar to those of SNe 2011fe and 2015F. From this similarity in late-time luminosity, we conclude that the slight discrepancy in the masses of SN 2013aa and SN 2011fe is the result of missing data between 500-1000 days. Furthermore, we find no direct correlation between the values of stretch and $M(^{57}\text{Co})/M(^{56}\text{Co})$ measured in observed late-time SNe Ia to those of single-degenerate and double-degenerate explosion models. While the mass ratio and stretch of some late-time SNe Ia are comparable to that of particular explosion models e.g., SN 2013aa to a $1.1+0.9 M_{\odot}$ Violent Merger, or SN 2015F to a $0.9+0.76 M_{\odot}$ Violent Merger, there still exists no visible trend between data and models. The large spread between the predicted mass ratios of explosion models and those of observed late-time SNe indicates a need for either a more comprehensive model analysis of the physics behind supernova explosions, or the reduction of systematic errors in determining the luminosities of late-time SNe Ia. Additional observations of SN 2013aa should improve both mass estimates and mitigate potential systematic effects.

6 Tables

Table 5. Explosion Model Characteristics

Model	Description	Density (g cm^{-3})	$M(\text{WD})$ (M_{\odot})	$M(^{56}\text{Ni})$ (M_{\odot})	$^{57}\text{Co}/^{56}\text{Co}$	Stretch	Ref.
Single Degenerate							
W7	Deflagration	2×10^9	1.38	0.59	0.041	0.90	Iwamoto et al. (1999) [25]
ddt_n100	Delayed Detonation	2.9×10^9	1.40	0.60	0.031	0.83	Seitenzahl et al. (2013) [34]
det_1.06	Detonation	4.2×10^7	1.06	0.56	0.006	0.75	Sim et al. (2010) [70]
doublett_CSDDD-S	Double Detonation	8.5×10^6	0.79	0.21	0.044	0.89	Sim et al. (2012) [71]
def_N100def	Pure Deflagration	2.9×10^9	1.40	0.36	0.038	0.84	Fink et al. (2014) [72]
det_ONe15e7	O-Ne WD Detonation	1.5×10^8	1.23	0.96	0.009	0.79	Marquardt et al. (2015) [73]
gcd_GCID200	Detonation	1.0×10^6	1.40	0.74	0.025	0.92	Seitenzahl et al. (2016) [74]
Double Degenerate							
merger_11+09	Violent Merger	2.0×10^6	$1.10 + 0.90$	0.10	0.024	1.03	Pakmor et al. (2012) [30]
merger_09+09	Violent Merger	3.8×10^6	$0.90 + 0.90$	0.10	0.003	0.80	Pakmor et al. (2010) [75]
merger_09+076_Z1	Violent Merger	2.0×10^6	$0.90 + 0.76$	0.18	0.009	0.89	Kromer et al. (2013) [76]

Table 5 (cont'd)

Model	Description	Density (g cm^{-3})	M(WD) (M_{\odot})	M(^{56}Ni) (M_{\odot})	$^{57}\text{Co}/^{56}\text{Co}$	Stretch	Ref.
merger_09+076_Z0.01	Violent Merger	2.0×10^6	$0.90 + 0.76$	0.18	0.003	0.99	Kromer et al. (2016) [77]

Bibliography

- [1] F. Hoyle and W. A. Fowler, **132**, 565 (1960).
- [2] A. G. Riess, W. H. Press, and R. P. Kirshner, **473**, 88 (1996).
- [3] A. G. Riess, A. V. Filippenko, P. Challis, A. Clocchiatti, A. Diercks, P. M. Garnavich, R. L. Gilliland, C. J. Hogan, S. Jha, R. P. Kirshner, B. Leibundgut, M. M. Phillips, D. Reiss, B. P. Schmidt, R. A. Schommer, R. C. Smith, J. Spyromilio, C. Stubbs, N. B. Suntzeff, and J. Tonry, **116**, 1009 (1998).
- [4] S. Perlmutter, G. Aldering, G. Goldhaber, R. A. Knop, P. Nugent, P. G. Castro, S. Deustua, S. Fabbro, A. Goobar, D. E. Groom, I. M. Hook, A. G. Kim, M. Y. Kim, J. C. Lee, N. J. Nunes, R. Pain, C. R. Pennypacker, R. Quimby, C. Lidman, R. S. Ellis, M. Irwin, R. G. McMahon, P. Ruiz-Lapuente, N. Walton, B. Schaefer, B. J. Boyle, A. V. Filippenko, T. Matheson, A. S. Fruchter, N. Panagia, H. J. M. Newberg, W. J. Couch, and T. S. C. Project, **517**, 565 (1999).
- [5] S. A. Colgate and C. McKee, **157**, 623 (1969).
- [6] S. E. Woosley and T. A. Weaver, **24**, 205 (1986).
- [7] W. Li, J. Leaman, R. Chornock, A. V. Filippenko, D. Poznanski, M. Ganeshalingam, X. Wang, M. Modjaz, S. Jha, R. J. Foley, and N. Smith, **412**, 1441 (2011).
- [8] A. V. Filippenko, **101**, 588 (1989).
- [9] D. Branch and S. van den Bergh, **105**, 2231 (1993).

- [10] M. Hamuy, M. M. Phillips, N. B. Suntzeff, R. A. Schommer, J. Maza, R. C. Smith, P. Lira, and R. Aviles, **112**, 2438 (1996).
- [11] M. Childress, G. Aldering, P. Antilogus, C. Aragon, S. Bailey, C. Baltay, S. Bongard, C. Buton, A. Canto, F. Cellier-Holzem, N. Chotard, Y. Copin, H. K. Fakhouri, E. Gangler, J. Guy, E. Y. Hsiao, M. Kerschhaggl, A. G. Kim, M. Kowalski, S. Loken, P. Nugent, K. Paech, R. Pain, E. Pecontal, R. Pereira, S. Perlmutter, D. Rabinowitz, M. Rigault, K. Runge, R. Scalzo, G. Smadja, C. Tao, R. C. Thomas, B. A. Weaver, and C. Wu, **770**, 108 (2013).
- [12] W. Li, J. Leaman, R. Chornock, A. V. Filippenko, D. Poznanski, M. Ganeshalingam, X. Wang, M. Modjaz, S. Jha, R. J. Foley, and N. Smith, **412**, 1441 (2011).
- [13] M. M. Phillips, **413**, L105 (1993).
- [14] A. G. Kim, S. Gabi, G. Goldhaber, D. E. Groom, I. M. Hook, M. Y. Kim, J. C. Lee, C. R. Pennypacker, S. Perlmutter, I. A. Small, A. Goobar, R. Pain, R. S. Ellis, R. G. McMahon, B. J. Boyle, P. S. Bunclark, D. Carter, M. J. Irwin, K. Glazebrook, H. J. M. Newberg, A. V. Filippenko, T. Matheson, M. Dopita, W. J. Couch, and . S. C. Project), **476**, L63 (1997).
- [15] S. Taubenberger, ArXiv e-prints (2017).
- [16] S. Perlmutter, S. Gabi, G. Goldhaber, A. Goobar, D. E. Groom, I. M. Hook, A. G. Kim, M. Y. Kim, J. C. Lee, R. Pain, C. R. Pennypacker, I. A. Small, R. S. Ellis, R. G. McMahon, B. J. Boyle, P. S. Bunclark, D. Carter, M. J. Irwin, K. Glazebrook, H. J. M. Newberg, A. V. Filippenko, T. Matheson, M. Dopita, and W. J. Couch, **483**, 565 (1997).
- [17] G. Goldhaber, D. E. Groom, A. Kim, G. Aldering, P. Astier, A. Conley, S. E. Deustua, R. Ellis, S. Fabbro, A. S. Fruchter, A. Goobar, I. Hook, M. Irwin, M. Kim, R. A. Knop, C. Lidman, R. McMahon, P. E. Nugent, R. Pain, N. Panagia, C. R. Pennypacker, S. Perlmutter, P. Ruiz-Lapuente, B. Schaefer, N. A. Walton, and T. York, **558**, 359 (2001).
- [18] D. Maoz, F. Mannucci, and G. Nelemans, **52**, 107 (2014).

- [19] S. E. Woosley, R. E. Taam, and T. A. Weaver, **301**, 601 (1986).
- [20] A. Heger, C. L. Fryer, S. E. Woosley, N. Langer, and D. H. Hartmann, **591**, 288 (2003).
- [21] P. A. Mazzali, F. K. Röpke, S. Benetti, and W. Hillebrandt, *Science* **315**, 825 (2007).
- [22] A. L. Piro and P. Chang, **678**, 1158 (2008).
- [23] I. Iben, Jr. and A. V. Tutukov, **54**, 335 (1984).
- [24] S. E. Woosley, S. Wunsch, and M. Kuhlen, **607**, 921 (2004).
- [25] K. Iwamoto, F. Brachwitz, K. Nomoto, N. Kishimoto, H. Umeda, W. R. Hix, and F.-K. Thielemann, **125**, 439 (1999).
- [26] I. R. Seitenzahl, G. Cescutti, F. K. Röpke, A. J. Ruiter, and R. Pakmor, **559**, L5 (2013).
- [27] F. K. Röpke, M. Kromer, I. R. Seitenzahl, R. Pakmor, S. A. Sim, S. Taubenberger, F. Ciaraldi-Schoolmann, W. Hillebrandt, G. Aldering, P. Antilogus, C. Baltay, S. Benitez-Herrera, S. Bongard, C. Buton, A. Canto, F. Cellier-Holzem, M. Childress, N. Chotard, Y. Copin, H. K. Fakhouri, M. Fink, D. Fouchez, E. Gangler, J. Guy, S. Hachinger, E. Y. Hsiao, J. Chen, M. Kerschhaggl, M. Kowalski, P. Nugent, K. Paech, R. Pain, E. Pecontal, R. Pereira, S. Perlmutter, D. Rabinowitz, M. Rigault, K. Runge, C. Saunders, G. Smadja, N. Suzuki, C. Tao, R. C. Thomas, A. Tilquin, and C. Wu, **750**, L19 (2012).
- [28] A. M. Khokhlov, **245**, 114 (1991).
- [29] J. Whelan and I. Iben, Jr., **186**, 1007 (1973).
- [30] R. Pakmor, M. Kromer, S. Taubenberger, S. A. Sim, F. K. Röpke, and W. Hillebrandt, **747**, L10 (2012).
- [31] R. F. Webbink, **277**, 355 (1984).
- [32] K. Maguire, S. Taubenberger, M. Sullivan, and P. A. Mazzali, **457**, 3254 (2016).

- [33] L. Chomiuk, A. M. Soderberg, R. A. Chevalier, S. Bruzewski, R. J. Foley, J. Parrent, J. Strader, C. Badenes, C. Fransson, A. Kamble, R. Margutti, M. P. Rupen, and J. D. Simon, **821**, 119 (2016).
- [34] I. R. Seitenzahl, F. Ciaraldi-Schoolmann, F. K. Röpkke, M. Fink, W. Hillebrandt, M. Kromer, R. Pakmor, A. J. Ruiter, S. A. Sim, and S. Taubenberger, **429**, 1156 (2013).
- [35] W. D. Arnett, **253**, 785 (1982).
- [36] I. R. Seitenzahl and D. M. Townsley, ArXiv e-prints (2017).
- [37] I. R. Seitenzahl, S. Taubenberger, and S. A. Sim, **400**, 531 (2009).
- [38] D. Kasen and P. E. Nugent, Annual Review of Nuclear and Particle Science **63**, 153 (2013).
- [39] B. J. Shappee, K. Z. Stanek, C. S. Kochanek, and P. M. Garnavich, **841**, 48 (2017).
- [40] G. Dimitriadis, M. Sullivan, W. Kerzendorf, A. J. Ruiter, I. R. Seitenzahl, S. Taubenberger, G. B. Doran, A. Gal-Yam, R. R. Laher, K. Maguire, P. Nugent, E. O. Ofek, and J. Surace, **468**, 3798 (2017).
- [41] O. Graur, D. Zurek, M. M. Shara, A. G. Riess, I. R. Seitenzahl, and A. Rest, **819**, 31 (2016).
- [42] Y. Yang, L. Wang, D. Baade, P. J. Brown, A. Cikota, M. Cracraft, P. A. Hoflich, J. Maund, F. Patat, W. B. Sparks, J. Spyromilio, H. F. Stevance, X. Wang, and J. C. Wheeler, ArXiv e-prints (2017).
- [43] O. Graur, D. R. Zurek, A. Rest, I. R. Seitenzahl, B. J. Shappee, R. Fisher, J. Guillochon, M. M. Shara, and A. G. Riess, ArXiv e-prints (2017).
- [44] S. Parker, A. Amorim, J. T. Parrent, D. Sand, S. Valenti, M. L. Graham, and D. A. Howell, Central Bureau Electronic Telegrams **3416**, (2013).
- [45] J. T. Parrent, D. Sand, S. Valenti, M. J. Graham, and D. A. Howell, The Astronomer's Telegram **4817**, (2013).

- [46] M. L. Graham, S. Kumar, G. Hosseinzadeh, D. Hiramatsu, I. Arcavi, D. A. Howell, S. Valenti, D. J. Sand, J. T. Parrent, C. McCully, and A. V. Filippenko, ArXiv e-prints (2017).
- [47] J. Guy, P. Astier, S. Baumont, D. Hardin, R. Pain, N. Regnault, S. Basa, R. G. Carlberg, A. Conley, S. Fabbro, D. Fouchez, I. M. Hook, D. A. Howell, K. Perrett, C. J. Pritchett, J. Rich, M. Sullivan, P. Antilogus, E. Aubourg, G. Bazin, J. Bronder, M. Filiol, N. Palanque-Delabrouille, P. Ripoche, and V. Ruhlmann-Kleider, **466**, 11 (2007).
- [48] T. M. Brown, N. Baliber, F. B. Bianco, M. Bowman, B. Burleson, P. Conway, M. Crellin, É. Depagne, J. De Vera, B. Dilday, D. Dragomir, M. Dubberley, J. D. Eastman, M. Elphick, M. Falarski, S. Foale, M. Ford, B. J. Fulton, J. Garza, E. L. Gomez, M. Graham, R. Greene, B. Haldeman, E. Hawkins, B. Haworth, R. Haynes, M. Hidas, A. E. Hjelstrom, D. A. Howell, J. Hygelund, T. A. Lister, R. Lobdill, J. Martinez, D. S. Mullins, M. Norbury, J. Parrent, R. Paulson, D. L. Petry, A. Pickles, V. Posner, W. E. Rosing, R. Ross, D. J. Sand, E. S. Saunders, J. Shobbrook, A. Shporer, R. A. Street, D. Thomas, Y. Tsapras, J. R. Tufts, S. Valenti, K. Vander Horst, Z. Walker, G. White, and M. Willis, **125**, 1031 (2013).
- [49] P. J. Brown, A. A. Breeveld, S. Holland, P. Kuin, and T. Pritchard, **354**, 89 (2014).
- [50] R. L. Davies, J. R. Allington-Smith, P. Bettess, E. Chadwick, R. Content, G. N. Dodsworth, R. Haynes, D. Lee, I. J. Lewis, J. Webster, E. Atad, S. M. Beard, M. Ellis, P. R. Hastings, P. R. Williams, T. Bond, D. Crampton, T. J. Davidge, M. Fletcher, B. Leckie, C. L. Morbey, R. G. Murowinski, S. Roberts, L. K. Saddlemyer, J. Sebesta, J. R. Stilburn, and K. Szeto, in *Optical Telescopes of Today and Tomorrow*, Vol. 2871 of , edited by A. L. Ardeberg (PUBLISHER, ADDRESS, 1997), pp. 1099–1106.
- [51] A. Conley, M. Sullivan, E. Y. Hsiao, J. Guy, P. Astier, D. Balam, C. Balland, S. Basa, R. G. Carlberg, D. Fouchez, D. Hardin, D. A. Howell, I. M. Hook, R. Pain, K. Perrett, C. J. Pritchett, and N. Regnault, **681**, 482 (2008).

- [52] M. J. Childress, D. J. Hillier, I. Seitenzahl, M. Sullivan, K. Maguire, S. Taubenberger, R. Scalzo, A. Ruiter, N. Blagorodnova, Y. Camacho, J. Castillo, N. Elias-Rosa, M. Fraser, A. Gal-Yam, M. Graham, D. A. Howell, C. Inserra, S. W. Jha, S. Kumar, P. A. Mazzali, C. McCully, A. Morales-Garoffolo, V. Pandya, J. Polshaw, B. Schmidt, S. Smartt, K. W. Smith, J. Sollerman, J. Spyromilio, B. Tucker, S. Valenti, N. Walton, C. Wolf, O. Yaron, D. R. Young, F. Yuan, and B. Zhang, **454**, 3816 (2015).
- [53] O. Yaron and A. Gal-Yam, **124**, 668 (2012).
- [54] S. Blondin and J. L. Tonry, **666**, 1024 (2007).
- [55] D. A. Howell, M. Sullivan, K. Perrett, T. J. Bronder, I. M. Hook, P. Astier, E. Aubourg, D. Balam, S. Basa, R. G. Carlberg, S. Fabbro, D. Fouchez, J. Guy, H. Lafoux, J. D. Neill, R. Pain, N. Palanque-Delabrouille, C. J. Pritchett, N. Regnault, J. Rich, R. Taillet, R. Knop, R. G. McMahon, S. Perlmutter, and N. A. Walton, **634**, 1190 (2005).
- [56] R. Foley, 4 For 1: UV Spectroscopy of a Young, Nearby SN Ia, Cepheid Distances to 2 SN Ia, and Extremely Late-time Photometry of Another SN Ia, HST Proposal, 2016.
- [57] S. Gonzaga and et al., *The DrizzlePac Handbook, HST Data Handbook* (PUBLISHER, ADDRESS, 2012).
- [58] A. E. Dolphin, **112**, 1383 (2000).
- [59] W. E. Kerzendorf, C. McCully, S. Taubenberger, A. Jerkstrand, I. Seitenzahl, A. J. Ruiter, J. Spyromilio, K. S. Long, and C. Fransson, **472**, 2534 (2017).
- [60] J. A. Cardelli, G. C. Clayton, and J. S. Mathis, **345**, 245 (1989).
- [61] E. Y. Hsiao, A. Conley, D. A. Howell, M. Sullivan, C. J. Pritchett, R. G. Carlberg, P. E. Nugent, and M. M. Phillips, **663**, 1187 (2007).

- [62] S. Taubenberger, N. Elias-Rosa, W. E. Kerzendorf, S. Hachinger, J. Spyromilio, C. Fransson, M. Kromer, A. J. Ruiter, I. R. Seitenzahl, S. Benetti, E. Cappellaro, A. Pastorello, M. Turatto, and A. Marchetti, **448**, L48 (2015).
- [63] J. Sollerman, J. Lindahl, C. Kozma, P. Challis, A. V. Filippenko, C. Fransson, P. M. Garnavich, B. Leibundgut, W. Li, P. Lundqvist, P. Milne, J. Spyromilio, and R. P. Kirshner, **428**, 555 (2004).
- [64] M. Stritzinger and J. Sollerman, **470**, L1 (2007).
- [65] G. Leloudas, M. D. Stritzinger, J. Sollerman, C. R. Burns, C. Kozma, K. Krisciunas, J. R. Maund, P. Milne, A. V. Filippenko, C. Fransson, M. Ganeshalingam, M. Hamuy, W. Li, M. M. Phillips, B. P. Schmidt, J. Skottfelt, S. Taubenberger, L. Boldt, J. P. U. Fynbo, L. Gonzalez, M. Salvo, and J. Thomas-Osip, **505**, 265 (2009).
- [66] R. Pereira, R. C. Thomas, G. Aldering, P. Antilogus, C. Baltay, S. Benitez-Herrera, S. Bongard, C. Buton, A. Canto, F. Cellier-Holzem, J. Chen, M. Childress, N. Chotard, Y. Copin, H. K. Fakhouri, M. Fink, D. Fouchez, E. Gangler, J. Guy, W. Hillebrandt, E. Y. Hsiao, M. Kerschhaggl, M. Kowalski, M. Kromer, J. Nordin, P. Nugent, K. Paech, R. Pain, E. Pécontal, S. Perlmutter, D. Rabinowitz, M. Rigault, K. Runge, C. Saunders, G. Smadja, C. Tao, S. Taubenberger, A. Tilquin, and C. Wu, **554**, A27 (2013).
- [67] C. Fransson and A. Jerkstrand, **814**, L2 (2015).
- [68] D. Foreman-Mackey, D. W. Hogg, D. Lang, and J. Goodman, **125**, 306 (2013).
- [69] S. T. Ohlmann, M. Kromer, M. Fink, R. Pakmor, I. R. Seitenzahl, S. A. Sim, and F. K. Röpke, **572**, A57 (2014).
- [70] S. A. Sim, F. K. Röpke, W. Hillebrandt, M. Kromer, R. Pakmor, M. Fink, A. J. Ruiter, and I. R. Seitenzahl, **714**, L52 (2010).

- [71] S. A. Sim, M. Fink, M. Kromer, F. K. Röpke, A. J. Ruiter, and W. Hillebrandt, **420**, 3003 (2012).
- [72] M. Fink, M. Kromer, I. R. Seitzzahl, F. Ciaraldi-Schoolmann, F. K. Röpke, S. A. Sim, R. Pakmor, A. J. Ruiter, and W. Hillebrandt, **438**, 1762 (2014).
- [73] K. S. Marquardt, S. A. Sim, A. J. Ruiter, I. R. Seitzzahl, S. T. Ohlmann, M. Kromer, R. Pakmor, and F. K. Röpke, **580**, A118 (2015).
- [74] I. R. Seitzzahl, M. Kromer, S. T. Ohlmann, F. Ciaraldi-Schoolmann, K. Marquardt, M. Fink, W. Hillebrandt, R. Pakmor, F. K. Röpke, A. J. Ruiter, S. A. Sim, and S. Taubenberger, **592**, A57 (2016).
- [75] R. Pakmor, M. Kromer, F. K. Röpke, S. A. Sim, A. J. Ruiter, and W. Hillebrandt, **463**, 61 (2010).
- [76] M. Kromer, R. Pakmor, S. Taubenberger, G. Pignata, M. Fink, F. K. Röpke, I. R. Seitzzahl, S. A. Sim, and W. Hillebrandt, **778**, L18 (2013).
- [77] M. Kromer, C. Fremling, R. Pakmor, S. Taubenberger, R. Amanullah, S. B. Cenko, C. Fransson, A. Goobar, G. Leloudas, F. Taddia, F. K. Röpke, I. R. Seitzzahl, S. A. Sim, and J. Sollerman, **459**, 4428 (2016).
- [78] G. P. Kuiper, **88**, 472 (1938).